International Journal of Multiphase Flow 67 (2014) 88–105

Contents lists available at ScienceDirect

International Journal of Multiphase Flow

journal homepage: www.elsevier.com/locate/ijmulflow

Numerical investigation of gravitational effects in horizontal annular liquid–gas flow

Jeremy O. McCaslin *, Olivier Desjardins

Sibley School of Mechanical and Aerospace Engineering, Cornell University, Ithaca, NY 14853, USA

ARTICLE INFO

Article history:
Received 12 May 2014
Received in revised form 14 August 2014
Accepted 18 August 2014
Available online 27 August 2014

Keywords:
Multiphase flow
Liquid–gas flow
Annular flow
Stratified flow
Direct numerical simulation
Film sustainment

ABSTRACT

In this work, exploratory numerical simulations of liquid–gas flows in horizontal pipes are conducted for three different sets of conditions in the annular and stratified-annular flow regimes. Careful dimensional analysis is used to choose governing parameters in a way that yields flows that are relevant to realistic engineering applications, while remaining computationally tractable. Statistics of the velocity field and height of the liquid film are computed as a function of circumferential location in the pipe, demonstrating the existence of a viscous sublayer within the liquid film, as well as a viscous layer near the interface and a log law region within the gas core. The probability of dry-out conditions at the wall in upper regions of the pipe is shown to increase as gravitational effects increase. Circumferential motion of the liquid and gas phases within the pipe cross section are analyzed, informing possible mechanisms for sustainment of the liquid film. A simple model is developed that helps to characterize the dynamics of the liquid annulus and aids in understanding the effect of secondary gas flow on the circumferential motion of the film. Void fraction, film height, and film asymmetry are compared with experimental correlations available in the literature.

Introduction

The concurrent flow of liquid and gas inside circular pipes occurs in a vast range of engineering devices, such as chemical and nuclear reactors, pipelines, oil wells, and the receiver tubes of direct steam generation, among others. Depending on the relevant governing dimensionless parameters, the distribution of the phase interface can take many different forms. The way in which the phases are distributed will significantly impact hydrodynamic and thermal properties of these flows, which will in turn affect the optimized operation conditions and economical design of such systems. In horizontal systems, gravitational effects lead to stratification, i.e., the buoyancy of the gas phase causes it to migrate to upper regions of the domain. This tendency can be diminished, depending on the relative importance of inertial and gravitational effects, as well as the gas volume fraction (also known as the void fraction). Within horizontal circular pipes, common flow regimes include bubbly flow, plug flow, slug flow, stratified and stratified-wavy flow, and annular and disperse–annular flow (Carey, 2008).

Details regarding global flow characteristics that lead to different multiphase flow regimes are provided by Carey (2008) and are briefly conveyed here. At small void fractions, bubbly flow is characteristically observed. Small bubbles coalesce as the void fraction increases, forming larger bubbles. Larger bubbles intermittently flow in the upper region of the pipe, characteristic of plug flow. If the void fraction is high and inertial effects are small, the gas and liquid fully separate and stratified flow occurs. Kelvin–Helmholtz type instabilities can occur in the stratified regime if the inertia of the gas is high enough, causing the interface between the phases to become wavy. The waves may reach the top of the pipe if their amplitude becomes large enough, taking a “slug-like” appearance, thus referred to as slug flow. When the void fraction is large and inertial effects dominate in the gas phase, an annular flow can occur in which the liquid assumes the form of a thin annular film around the interior surface of the pipe, while a gas core flows through the center. Buoyancy effects cause the film to be thinner near the top of the pipe than the bottom, leading to interfacial corrugations that vary in the circumferential direction due to waves that protrude further into the gas core near lower regions of the pipe. Shear caused by the high-inertia gas also has a tendency to entrain liquid droplets into the gas core. The aforementioned flow regimes for horizontal gas–liquid flows can be difficult to distinguish from one another, as transitional forms of these regimes are common. In the past half-century, much work has gone into developing flow pattern maps in order to predict

* Corresponding author.
E-mail address: jom48@cornell.edu (J.O. McCaslin).

http://dx.doi.org/10.1016/j.ijmultiphaseflow.2014.08.006
0301-9322/

flow regimes based on important flow parameters (Alves, 1954; Baker, 1953; Ghajar et al., 2007; Hoogendoorn, 1959; Kosterin, 1949; Krasiakova, 1957; Mandhane et al., 1974; Taitel and Dukler, 1976). These maps aim to categorize the two-phase flow into the discussed regimes based on characteristics of the phases, such as superficial velocities and Reynolds numbers. Some maps have had more success than others, but it is difficult for any two parameters to contain enough information about the two-phase flow to determine the resulting interfacial distribution.

Annular flows are especially common under conditions relevant to a plethora of thermo-fluid transport systems, and have therefore received much attention from experiments. A common goal of many experiments has been to extract the liquid film thickness, measured through planar laser-induced fluorescence (Schubring et al., 2010a,b; Farias et al., 2011), conductance probes (Hagiwara et al., 1989; Paras and Karabelas, 1991a), fast response X-ray tomography (Hu et al., 2013), and other techniques (Laurinat et al., 1985; Hewitt et al., 1990; Hurlburt and Newell, 1996, 2000; Shedd and Newell, 2004; Schubring and Shedd, 2008). Other workers have measured mean circumferential velocity through photochromic dye activation (Sutharshan et al., 1995). A range of other quantities relevant for practical applications have also been measured extensively, such as wall shear (Hagiwara et al., 1989; Schubring and Shedd, 2009a) and pressure drop (Shedd and Newell, 2004; Schubring and Shedd, 2008). Multiphase dynamics that pertain to film sustainment mechanisms have been measured, such as characteristics of droplet entrainment and deposition (Paras and Karabelas, 1991b; Azzopardi, 1999; Al-Sarkhi and Hanratty, 2002; Rodriguez et al., 2004; Alekseenko et al., 2013), induced secondary gas circulation (Flores et al., 1995), and surface wave characteristics (Jayanti et al., 1990a; Hurlburt and Newell, 1996; Schubring and Shedd, 2008). Despite efforts to formulate theories and models to predict flow regime characteristics and regime transitions (Jacowitz et al., 1964; Anderson and Russel, 1970; Taitel and Dukler, 1976; Kadambi, 1982; Ooms et al., 1983; Fukano and Ousaka, 1989; Serdar Kaya et al., 2000; Ooms and Poesio, 2003; Adechy, 2004; Moreno Quibén and Thome, 2007; Schubring et al., 2011; Al-Sarkhi et al., 2012; Öztürk et al., 2013), there is a lack of theoretical understanding that would allow for a description of the interface distribution from first principles.

Numerical studies of multiphase flows in transport systems are very limited in comparison with their experimental counterparts. The vast majority of relevant liquid–gas direct numerical simulations (DNS) have focused on bubbly flows (Esmaeeli and Tryggvason, 1998, 1999; Bunner and Tryggvason, 1999, 2002a,b; Nagrath et al., 2005), while significantly less computations of other regimes have been performed. Those that do exist often rely on a simplified models to account for relevant physical processes, such as two- and multi-fluid model-based simulations of slug flow (Issa and Kempf, 2003; Bonizzi and Issa, 2003a) and arising mechanisms for bubble entrainment (Bonizzi and Issa, 2003b). A number of numerical studies have been conducted that isolate a particular physical process that is relevant to a liquid–gas pipe flow, such as hydrodynamic counterbalancing of the buoyancy on the gas core (Ooms et al., 2007, 2012), DNS and large-eddy simulation (LES) of a sheared interface in turbulence (Fulgosi et al., 2003; Reboux et al., 2006), DNS of turbulent heat transfer across a sheared interface (Lakehal et al., 2003), LES and Reynolds-averaged Navier–Stokes (RANS) simulations of secondary flow effects on droplet deposition and turbophoresis (Jayanti et al., 1990b; van't Westende et al., 2007), two-dimensional simulation of wave entrainment in vertical pipes (Han and Gabriel, 2007), and simulation of liquid film formation through wave pumping (Fukano and Inatomi, 2003).

These types of numerical studies are very useful for gaining insight toward the important dynamics of liquid–gas pipe flows, yet computational limitations have prevented the formulation of a detailed, first principles-based study of a horizontal liquid–gas flow inside a pipe that combines a fully turbulent gas phase with the effects of a deformable interface and non-unity density and viscosity ratios. The present work is an exploratory investigation that seeks to combine all of these effects together, demonstrating that simulations of annular and stratified flows relevant to realistic engineering applications are computationally feasible if governing parameters are chosen carefully. The aim of the present study is to further understand the hydrodynamic conditions that delineate the annular and stratified flow regimes, and to test if the present numerical approach is capable of capturing the transition between these regimes.

The computational approach used in the current study is outlined in 'Computational approach', including a discussion of the governing equations and the methodology for interface capture. The system configuration is provided in 'System configuration', describing the simulation domain and the flow forcing mechanism, as well as validating the mesh resolution and immersed boundary method. Results of the simulations are discussed in 'Results', providing a wide range of computed statistics and comparison with experimental data and correlations. Mechanisms for film sustainment are discussed in 'Dynamics in the pipe cross section', followed by a simple model for the liquid film provided in 'A model for the liquid film' to further aid in understanding the interfacial dynamics as they pertain to film replenishment.

Computational approach

Mathematical formulation

The two-phase annular flows in this study are described by the continuity and Navier–Stokes equations. Assuming incompressibility of both phases, i.e., $\nabla \cdot \boldsymbol{u} = 0$, the continuity equation is written

$$\frac{D\rho}{Dt} = \frac{\partial \rho}{\partial t} + \boldsymbol{u} \cdot \nabla \rho = 0, \tag{1}$$

where $\boldsymbol{u}$ is the velocity field and ρ is the fluid density. The Navier–Stokes equations are written as

$$\frac{\partial \rho \boldsymbol{u}}{\partial t} + \nabla \cdot (\rho \boldsymbol{u} \otimes \boldsymbol{u}) = -\nabla p + \nabla \cdot \left(\mu\left[\nabla \boldsymbol{u} + \nabla \boldsymbol{u}^{\mathsf{T}}\right]\right) + \rho \boldsymbol{g} + \boldsymbol{f}_b, \tag{2}$$

where p is the pressure, $\boldsymbol{g}$ is the gravitational acceleration, and μ is the dynamic viscosity. The body force $\boldsymbol{f}_b$ used for momentum forcing within the periodic computational domain will be discussed in 'Flow forcing'.

The material properties are taken to be constant within each phase, and the subscripts l and g are used to describe the density and the viscosity in the liquid and gas, respectively. These quantities are discontinuous across the interface Γ, and it is convenient to introduce their jump as $[\rho]_\Gamma = \rho_l - \rho_g$ and $[\mu]_\Gamma = \mu_l - \mu_g$. The velocity field is continuous across Γ in the absence of phase change, i.e., $[\boldsymbol{u}]_\Gamma = 0$. This is valid for the isothermal conditions simulated herein. The surface tension force will lead to a discontinuity in the normal stress at the gas–liquid interface, which translates into a pressure jump that can be written as

$$[p]_\Gamma = \sigma\kappa + 2[\mu]_\Gamma \boldsymbol{n}^{\mathsf{T}} \cdot \nabla \boldsymbol{u} \cdot \boldsymbol{n}, \tag{3}$$

where σ is the surface tension coefficient, κ is the curvature of the interface, and $\boldsymbol{n}$ is the normal vector at the interface. The discontinuous pressure is dealt with using the ghost fluid method (GFM) (Fedkiw et al., 1999), and information regarding numerical implementation of these equations is given by Desjardins et al. (2008a,b).

Interface capturing

In this work, the accurate conservative level set approach (ACLS) of Desjardins et al. (2008b) is used to capture the phase interface, along with a discontinuous Galerkin discretization described by Owkes and Desjardins (2013). Within the level set framework, the interface is implicitly defined as an iso-surface of a smooth function ψ, and is transported by solving

$$\frac{\partial \psi}{\partial t} + \nabla \cdot (\boldsymbol{u}\psi) = 0. \tag{4}$$

Since the velocity field is solenoidal, this equation implies that the interface undergoes material transport, in accordance with Eq. (1). The level set function is defined as the hyperbolic tangent profile

$$\psi(\boldsymbol{x}, t) = \frac{1}{2}\left(\tanh\left(\frac{\phi(\boldsymbol{x}, t)}{2\varepsilon}\right) + 1\right), \tag{5}$$

where ε determines the thickness of the profile. In ACLS (Desjardins et al., 2008b), ε is set to half the computational cell size. From the previous equation, ϕ is a standard signed distance function, i.e.,

$$\phi(\boldsymbol{x}, t) = \pm\|\boldsymbol{x} - \boldsymbol{x}_\Gamma\|, \tag{6}$$

where $\boldsymbol{x}_\Gamma$ corresponds to the closest point on the interface from $\boldsymbol{x}$, and ϕ changes signs when Γ is crossed. The level set ψ must be re-initialized to preserve the hyperbolic tangent profile, as transport and numerical diffusion will distort it (McCaslin and Desjardins, 2014). Re-initialization is achieved by solving

$$\frac{\partial \psi}{\partial \tau} = \nabla \cdot (\varepsilon(\nabla\psi \cdot \boldsymbol{n})\boldsymbol{n}) - \nabla \cdot (\psi(1-\psi)\boldsymbol{n}), \tag{7}$$

where τ is a pseudo-time variable. Sequential solution of Eqs. (4) and (7) combines the accuracy of level set methods with excellent conservation properties. The details of the ACLS methodology and its coupling with the GFM are described elsewhere (Desjardins et al., 2008b; Owkes and Desjardins, 2013; Desjardins et al., 2013).

Immersed boundary method

The immersed boundary (IB) method used for the enclosing cylindrical geometry in the present study is based on the work of Meyer et al. (2010) and Desjardins et al. (2013) so that it provides discrete conservation of mass and momentum. To illustrate the basic IB methodology, consider a general conservative transport equation for a quantity ω, written as

$$\frac{\partial \omega}{\partial t} + \nabla \cdot \boldsymbol{F}(\omega) = 0, \tag{8}$$

where $\boldsymbol{F}(\omega)$ represents the flux of ω. Second order finite volume discretization of Eq. (8) leads to

$$\omega_c^{n+1} = \omega_c^n - \frac{\Delta t}{V}\sum_{f=1}^{N_f}\left(A_f \boldsymbol{F}_f^{n+1/2} \cdot \boldsymbol{n}_f\right), \tag{9}$$

where ω_c^n is the cell-mean value of ω at time t^n, Δt is the size of the time step, V is the cell volume, N_f is the number of cell faces, A_f is the area of the cell face, $\boldsymbol{F}_f$ is the face-mean flux, and $\boldsymbol{n}_f$ is the outward normal to the cell face. Because computational cells containing the geometry are cut by the immersed boundary, Eq. (9) should be modified to contain only the portion of the cell that contains fluid, i.e., is "outside" the immersed boundary. Replacing the cell volume and area by their wetted fractions, Eq. (9) becomes

$$\omega_c^{n+1} = \omega_c^n - \frac{\Delta t}{\alpha_w^v V}\left(\sum_{f=1}^{N_f}\left(\alpha_w^s A_f \boldsymbol{F}_f^{n+1/2} \cdot \boldsymbol{n}_f\right) + A_{\mathrm{IB}} \boldsymbol{F}_{\mathrm{IB}}^{n+1/2} \cdot \boldsymbol{n}_{\mathrm{IB}}\right), \tag{10}$$

where $\alpha_w^v = V_w/V$ is the cell wetted volume V_w divided by the cell volume V, and $\alpha_w^s = A_w/A_f$ is the cell face wetted area A_w divided by the cell face area A. The last term accounts for the flux of ω at the IB, with A_{IB} as the cell immersed area, $\boldsymbol{F}_{\mathrm{IB}}$ the mean flux along the IB, and $\boldsymbol{n}_{\mathrm{IB}}$ the outward normal to the IB. Calculating V_w, A_w, and A_{IB} requires knowing the location of the immersed boundary $\boldsymbol{x}_{\mathrm{IB}}$, which is specified implicitly through the use of the signed distance level set

$$B(\boldsymbol{x}) = \pm\|\boldsymbol{x} - \boldsymbol{x}_{\mathrm{IB}}\|. \tag{11}$$

The immersed boundary then corresponds to $B(\boldsymbol{x}) = 0$, and a change in the sign of $B(\boldsymbol{x})$ distinguishes the domain inside the boundary from the domain outside. Further details regarding this immersed boundary method can be found elsewhere (Desjardins et al., 2013; Meyer et al., 2010).

System configuration

Simulation domain

Despite the appeal of a cylindrical mesh for pipe flow simulations, cylindrical coordinates automatically increase orthoradial resolution near the pipe centerline and decrease it near the boundary. This is undesirable when simulating a relatively thin annular flow that contains important interfacial dynamics near the pipe wall. Combined with the presence of liquid drops entrained in the gas core, the present study lends itself to the use of a uniform mesh so that multiphase dynamics can be well resolved everywhere. To that end, we perform the simulations on a uniform Cartesian mesh and account for the enclosing pipe geometry with the IB method described in the previous section.

Flow forcing

Simulations of fully developed two-phase pipe flow are achieved by prescribing periodic boundary conditions in the axial direction, denoted by x. Momentum lost at the pipe walls is reintroduced in the form of the constant source term $\boldsymbol{f}_b = f_b\hat{\boldsymbol{e}}_x$ in Eq. (2), where $\hat{\boldsymbol{e}}_x$ is the axial unit vector. The value of f_b is chosen to maintain a given bulk Reynolds number of a corresponding single-phase flow with the same pipe diameter D and fluid properties as the gas phase, written as $\mathrm{Re} = UD/\nu$, where U is the bulk axial velocity and ν is the kinematic viscosity. Once Re is chosen, Prandtl's friction law for smooth pipes (Pope, 2000) is used to obtain the friction factor f. The relation $f_b = \rho U^2 f/(2D)$ is then used to obtain the value of f_b used to force the two-phase flow. For a thin annular flow that is dynamically dominated by a high inertia gas core, the superficial gas Reynolds number will be close in value to the single-phase Reynolds number that f_b would yield.

Mesh resolution

The computational domain is of size $5D \times D \times D$ and is composed of $N_x \times N_y \times N_z = 1280 \times 256 \times 256$ uniform grid cells. To ensure sufficient resolution for the two-phase simulations, we validate that the mesh, together with the IB method, is capable of resolving a single-phase turbulent flow that is forced by the same f_b used in the two-phase simulations. Fig. 1 shows a single-phase turbulent flow with $\mathrm{Re} = 5310$ on the same uniform mesh used in the two-phase simulations. Results compare favorably with the well-established DNS results of Fukagata and Kasagi (2002). Standard plus units u^+ and y^+ are used for the mean profile on the left. The rms velocity u^{rms} is shown on the right as a function of y^+, and the x, r, and θ components agree very well with the cylindrical DNS of Fukagata and Kasagi (2002).

The smallest interfacial length scales that arise are limited by surface tension, which is a controlled parameter in the simulations. We set σ to be as large as possible to allow for droplet entrainment

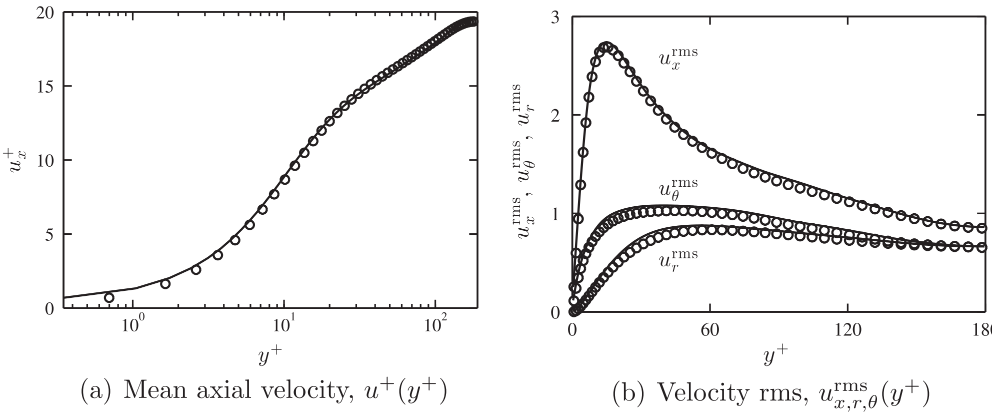

Fig. 1. Validation of the Cartesian mesh resolution with the immersed boundary method for a single-phase flow with $\mathrm{Re} = 5310$. NGA (Desjardins et al., 2008a) (lines), DNS of Fukagata and Kasagi (2002) on a cylindrical mesh (symbols).

Table 1
Fr_{sp} values for the three cases. Each case is run with $\mathrm{Re}_{sp} = 5000$, $\mathrm{We}_{sp} = 2000$, $f = 0.037$, $\rho_l/\rho_g = 16$, $\mu_l/\mu_g = 4.62$, and $\varepsilon_g = 0.85$. Gas phase properties correspond to air.

Case	Fr_{sp}
A	∞
B	6.56
C	1.64

into the gas core, but small enough to satisfy the condition that the mesh-based Weber number $\mathrm{We}_{\Delta x} = \rho_g u_{\rm rel}^2 \Delta x/\sigma \lesssim 5$, where Δx is the uniform mesh size. The relative velocity $u_{\rm rel}$ is estimated as the difference between the gas and liquid superficial velocities. This criterion corresponds to resolving vibrational breakup of a liquid droplet on at least two computational cells and should guarantee that most interfacial length scales are captured by the mesh.

Cases considered

The gaseous core in a horizontal annular flow must carry a significant amount of momentum in order to sustain a liquid film at the top of the pipe, since the liquid is much more dense. Thus, its velocity must be quite high. Indeed, very high gas Reynolds numbers are required to achieve an annular flow under realistic air–water type conditions, and such conditions are not computationally tractable with our approach. However, it is possible to obtain an annular flow in a simulation by modifying the density ratio, gas velocity, or gravitational acceleration. We do this carefully by defining the gas Froude number as

$$\mathrm{Fr}_g = \sqrt{\frac{\rho_g j_g^2}{\rho_l g D}}, \tag{12}$$

where j_g is the superficial gas velocity (described further below) and g is gravitational acceleration. The Froude number as defined in Eq. (12) is a measure of the ratio of aerodynamic forces from the gas phase to gravitational effects on the liquid phase. Simulations allow us to verify the idea that, assuming a large void fraction $\varepsilon_g = V_g/V$, which is the ratio of volume occupied by the gas phase V_g to the total volume V, a value of $\mathrm{Fr}_g \approx 1$ governs "annularity". Values of $\mathrm{Fr}_g > 1$ lead to the presence of a contiguous film, while $\mathrm{Fr}_g \lesssim 1$ means that the film is not contiguous around the pipe wall. The interfacial distribution converges to a stratified flow as $\mathrm{Fr}_g \to 0$.

Once the source term f_b is specified as described in 'Flow forcing', the other inputs to the simulations are the density and viscosity ratios, gravity, surface tension, and void fraction. Note that the wetted fraction $\varepsilon_l = 1 - \varepsilon_g$ is known when ε_g is known.

Since we do not know *a priori* what the value of j_g will be before the flow becomes statistically stationary, it is convenient to define the case parameters in terms of dimensionless variables based on the corresponding single-phase bulk velocity U:

$$\text{Reynolds number}: \quad \mathrm{Re}_{sp} = \frac{\rho_g U D}{\mu_g}, \tag{13}$$

$$\text{Weber number}: \quad \mathrm{We}_{sp} = \frac{\rho_g U^2 D}{\sigma}, \tag{14}$$

$$\text{Froude number}: \quad \mathrm{Fr}_{sp} = \sqrt{\frac{\rho_g U^2}{\rho_l g D}}, \tag{15}$$

$$\text{Friction factor}: \quad f = \frac{2 D f_b}{\rho_g U^2}. \tag{16}$$

In the present work we conduct three simulations with different values of Fr_{sp} to study the balance between inertia and gravity and test the capability of the computational approach to reproduce different flow regimes. Each case is simulated with $\mathrm{Re}_{sp} = 5000$, $\mathrm{We}_{sp} = 2000$, $f = 0.037$, $\rho_l/\rho_g = 16$, $\mu_l/\mu_g = 4.62$, and $\varepsilon_g = 0.85$. The value of Fr_{sp} for each case is provided in Table 1. The simulated density and viscosity ratios correspond to high pressure conditions inside the receiver tubes of direct steam generation loops, which is one application of interest for the present study.

Results

Flow characterization

Assuming an isothermal annular flow that is dynamically dominated by the high-inertia gas core, we use the following 3 dimensionless groups, in addition to $\mathrm{Fr}_g, \rho_l/\rho_g, \mu_l/\mu_g$, and ε_g, to characterize the flow:

$$\text{gas Reynolds number}: \quad \mathrm{Re}_g = \frac{\rho_g j_g D}{\mu_g}, \tag{17}$$

$$\text{gas Weber number}: \quad \mathrm{We}_g = \frac{\rho_g j_g^2 D}{\sigma}, \tag{18}$$

$$\text{flow quality}: \quad x = \frac{\dot{m}_g}{\dot{m}_g + \dot{m}_l}, \tag{19}$$

where $\dot{m}_{l,g}$ are the mass flow rates of the liquid and gas. The superficial gas velocity is defined as $j_g = \varepsilon_g u_g$, where the bulk gas velocity

$$u_g = \frac{\int_V \alpha_g u \, dV}{\int_V \alpha_g \, dV} = \frac{1}{V_g} \int_{V_g} u \, dV \tag{20}$$

is the axial velocity u averaged over the volume occupied by gas, and α_g is the local void fraction. Due to the presence of the liquid film, j_g is not equal to U, the bulk velocity in the single-phase case.

The flow quality, gas Reynolds number, gas Weber numer, and gas Froude number that the flow converges to depend on the balance between inertia and gravity and the resulting spatial distribution of the phase interface. Fig. 2 shows the convergence history of $\mathrm{Re}_g, \mathrm{We}_g, \mathrm{Fr}_g$, and x for the three simulations, and their converged values are listed in Table 2.

The nature of gravitational effects on the flow is clearly visible through inspection of Fig. 3. A large number of disperse drops exist within the gas core for both cases A and B, as is visible in Fig. 3(g) and (h). Drops are entrained and persist for a long time within the gas core before they are deposited on the liquid film, as gravitational effects are relatively limited compared to inertial effects for these cases. For case C, however, gravitational effects decrease the lifespan of drops within the gas core, returning them to the base film in lower regions of the pipe. This observation is in qualitative agreement with the experimental findings of Simmons and Hanratty (2001), who found that stratification of drops in a horizontal annular pipe diminished as gas velocity was increased, i.e., as inertia became more significant relative to gravitational effects. It is also evident in Fig. 3(a)–(f) that the circumferential bias of the liquid film thickness increases with decreasing Fr_g.

A first step to compare the simulations with experiments is made by plotting the simulations on the flow regime maps of Ghajar et al. (2007) and Taitel and Dukler (1976), as shown in Fig. 4(a) and (b), respectively. The regime map of Ghajar et al. (2007) shown in Fig. 4(a) is based on superficial phase Reynolds numbers and does not explicitly incorporate gravitational effects. The map was derived from air–water experiments (Ghajar et al., 2007) and therefore assumes a gravitational acceleration $g_0 = 9.81\ \mathrm{m/s^2}$. An annular flow requires a very large superficial gas velocity to yield a large Froude number based on g_0. Consequently, Re_g for cases B and C is not large enough to fall within the annular regime of the Ghajar et al. (2007) map, as seen in Fig. 4(a).

Table 2
Dimensionless groups for the three cases.

Case	x	Re_g	We_g	Fr_g
A	0.66	3.37×10^3	9.06×10^2	∞
B	0.70	3.48×10^3	9.67×10^2	4.56
C	0.65	3.65×10^3	1.07×10^3	1.20

The Taitel and Dukler (1976) map, however, does explicitly account for the effect of gravity. It is based on the Martinelli Factor X (Martinelli and Nelson, 1948) and the transition parameter F, defined as

$$X = \left(\frac{(dP/dx)_l}{(dP/dx)_g}\right)^{1/2} \tag{21}$$

and

$$F = \left(\frac{\rho_g j_g^2}{(\rho_l - \rho_g)Dg}\right)^{1/2}, \tag{22}$$

where $(dP/dx)_{l,g}$ are the frictional pressure gradients caused if the liquid or gas were flowing alone in the pipe. The values of $(dP/dx)_{l,g}$ are computed according to the formulation of Carey

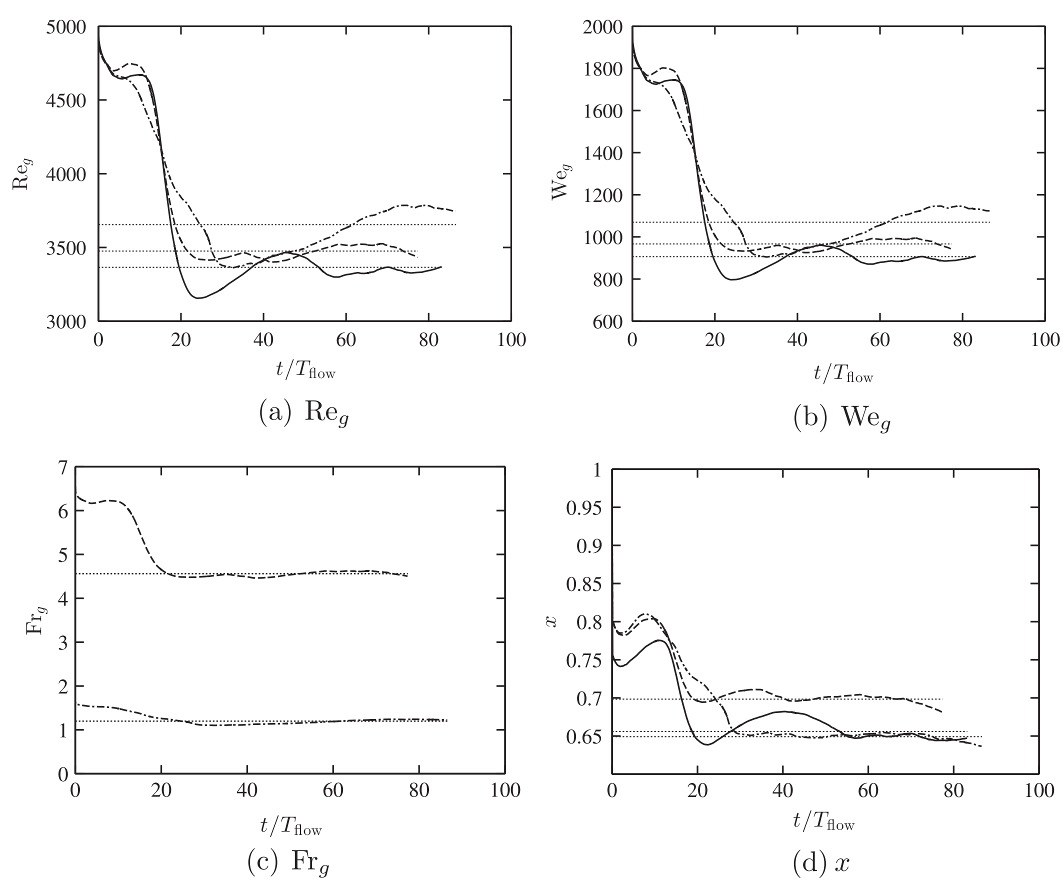

Fig. 2. Convergence history of $\mathrm{Re}_g, \mathrm{We}_g, \mathrm{Fr}_g$, and x. Simulation time t is normalized by T_{flow}, which is the flow through time of the gas core for the $\mathrm{Fr}_g = \infty$ case. $\mathrm{Fr}_g = \infty$ (solid line), $\mathrm{Fr}_g = 4.56$ (dashed line), $\mathrm{Fr}_g = 1.20$ (dash-dotted line). The thin dashed lines show the mean value computed over the assumed statistically stationary period.

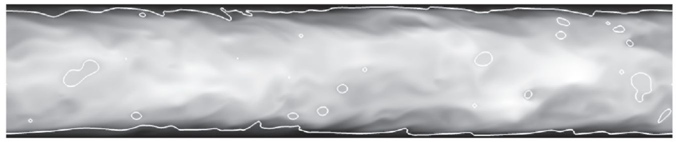

(a) Case A, side view

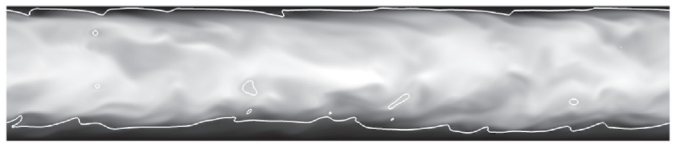

(b) Case B, side view

(c) Case C, side view

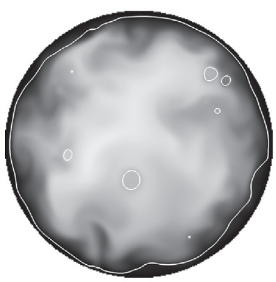

(d) Case A, front view

(e) Case B, front view

(f) Case C, front view

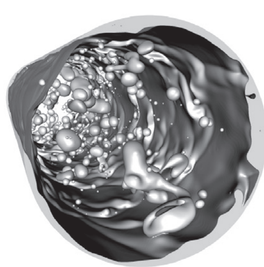

(g) Case A, 3D view

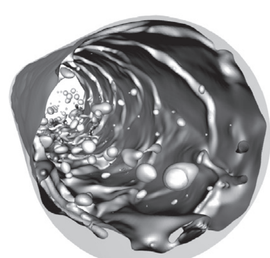

(h) Case B, 3D view

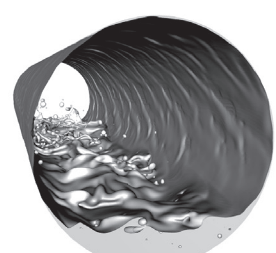

(i) Case C, 3D view

Fig. 3. Instantaneous results. In (a)–(f), the interface is shown by the white line, and the grayscale indicates normalized axial velocity, ranging from 0 (black) to 1.7 (white). The phase interface is shown in (g)–(i).

(2008) (see page 484 of Carey (2008)). Although both cases B and C fall within the disperse-annular regime of the Taitel and Dukler (1976) map in Fig. 4(b), the increased stratification of the film for case C is quantified by the fact that F is closer to the stratified-wavy regime for case C than for case B.

Liquid volume fraction statistics

To display radial profiles of the results, it is convenient to introduce the orthoradial angle θ, as defined in Fig. 5. For cases B and C in which $g \neq 0$, data is averaged about the plane of symmetry shown by the dashed line in Fig. 5. Fig. 6 compares the temporally and axially averaged liquid volume fraction $\alpha_l = 1 - \alpha_g$ for cases B and C, along with the mean location of the interface $h(\theta)$. While only slightly thicker near $\theta = 0$ for case B, the liquid film becomes significantly thicker for $0 \leqslant \theta \leqslant \pi/4$ in case C. This is also displayed in the profiles of $\alpha_l(y, \theta)$ in Fig. 7, where $y = R - r$ for a pipe of radius R with radial coordinate r. Although orthoradially symmetric, $\alpha_l(y, \theta)$ is shown for case A without averaging in θ for reference.

In industrial applications, much can be inferred about the two-phase dynamics of the pipe flow based on the void fraction. As a consequence, much effort has been put into developing experimental correlations and models for the void fraction (Butterworth, 1975; Harms et al., 2003; Serdar Kaya et al., 2000; Tandon et al., 1985) based on parameters such as quality and phase superficial velocities. A well-known correlation based solely on flow quality x and fluid densities is provided by Chisholm (1973), written as

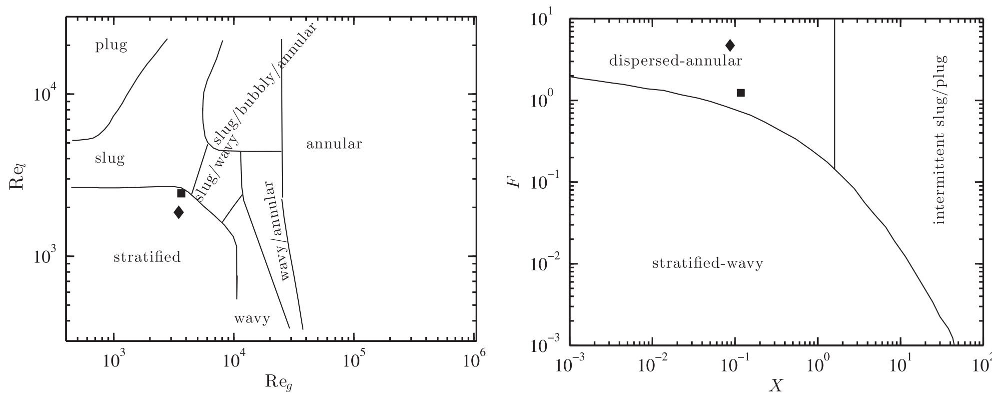

(a) Flow regime map of Ghajar and Tang (2007)

(b) Flow regime map of Taitel and Dukler (1976)

Fig. 4. Cases B and C on flow pattern maps found in the literature. Case B (♦), case C (■).

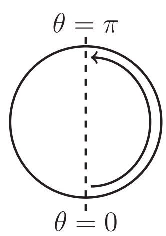

Fig. 5. Definition of orthoradial angle θ for flow statistics.

$$\varepsilon_{g,1}^{\mathrm{corr}} = \left[1 + \left(1 - x\left(1 - \frac{\rho_l}{\rho_g}\right)\right)^{1/2} \frac{\rho_g(1-x)}{\rho_l x}\right]^{-1}, \tag{23}$$

where the superscript "corr" denotes a correlated value. Table 3 shows the error between the prescribed void fraction $\varepsilon_g = 0.85$ compared to the correlated value for cases A–C, computed as

$$\mathrm{error} = \frac{\left|\varepsilon_{g,1}^{\mathrm{corr}} - \varepsilon_g\right|}{\varepsilon_g}, \tag{24}$$

and good agreement is observed.

A comprehensive assessment of 68 different experimental void fraction correlations proposed in the literature is provided by Woldesemayat and Ghajar (2007). Including the term proposed by Woldesemayat and Ghajar (2007) that accounts for pipe inclination angle β, the correlation of Coddington and Macian (2002) becomes

$$\varepsilon_{g,2}^{\mathrm{corr}} = j_g\left[j_g\left(1 + \left(\frac{j_l}{j_g}\right)^{(\rho_g/\rho_l)^{0.1}}\right) + 2.9\left(\frac{gD\sigma(1+\cos\beta)(\rho_l-\rho_g)}{\rho_l^2}\right)^{0.25}\right]^{-1}. \tag{25}$$

Table 4 shows the correlation error for each case, computed in the same way as Eq. (24). The correlation agrees reasonably well with the simulations, considering that 85.6% of the 2845 data points tested by Woldesemayat and Ghajar (2007) fall within 15% of the correlated value.

Velocity statistics

For case A in which the liquid film is not a function of θ, it is of interest to directly compare the single- and two-phase turbulent velocity profiles. Fig. 8(a) shows both profiles along with their corresponding viscous sublayers, which follow $u^+ = y^+$, and logarithmic regions, which follow

$$u^+ = \frac{1}{\kappa}\ln y^+ + c, \tag{26}$$

where κ is the von Kármán constant and c is a constant. The single-phase viscous sublayer roughly corresponds to the region $y^+ < 5$, while the logarithmic region corresponds to $y^+ > 30$. For the single-phase profile, Eq. (26) is plotted with $\kappa = 0.35$ and $c = 6$ in Fig. 8(a). Since the phase properties change across the interface,

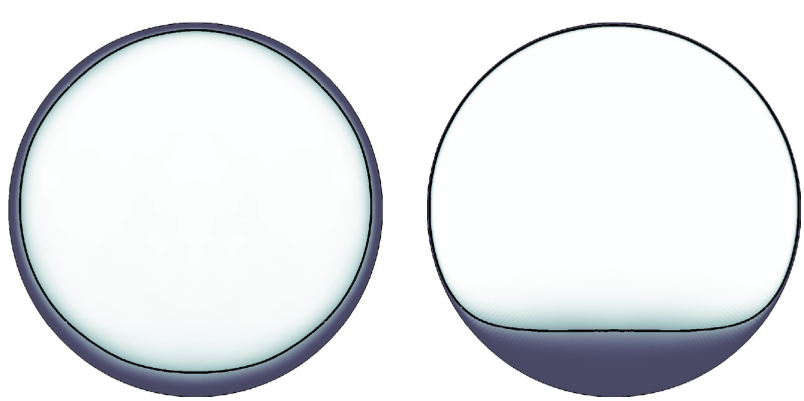

(a) Case B, α_l (b) Case C, α_l

Fig. 6. Mean α_l for cases B and C, varying from 0 (white) to 1 (gray). The mean location of the interface $h(\theta)$ is given by the black line.

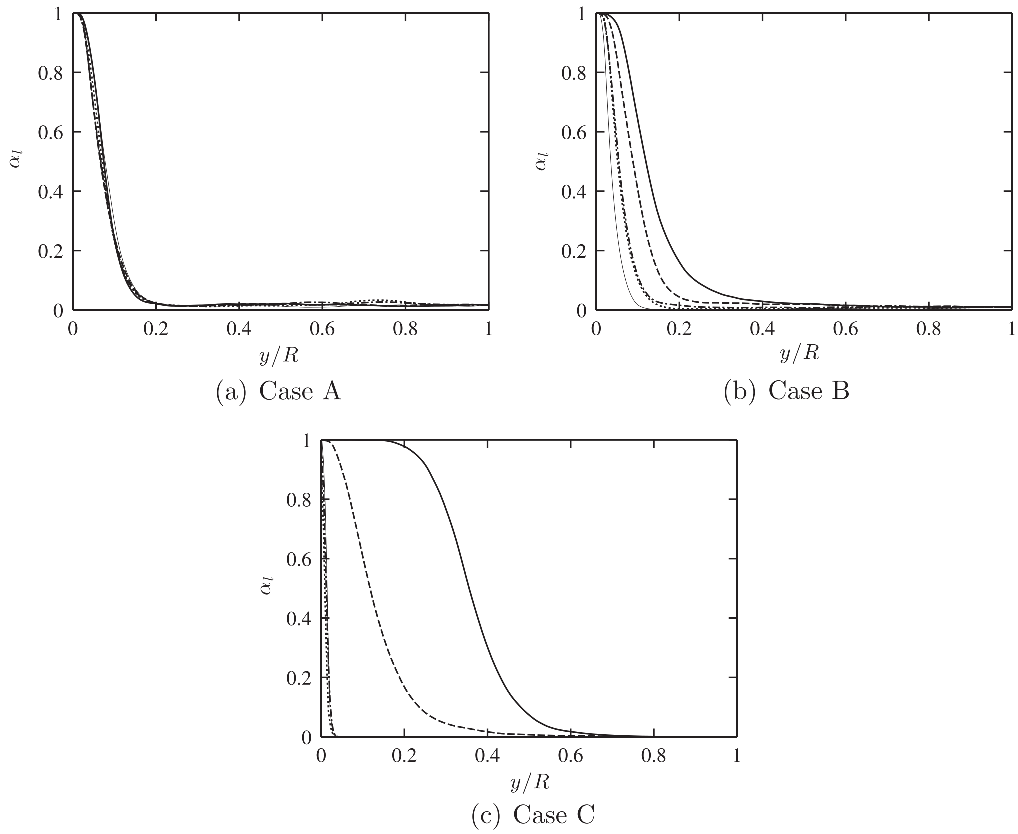

Fig. 7. Mean α_l as a function of y/R for different values of θ. $\theta/\pi = 0$ (thick solid line), $\theta/\pi = 1/4$ (dashed line), $\theta/\pi = 1/2$ (dash-dotted line), $\theta/\pi = 3/4$ (dotted line), $\theta/\pi = 1$ (thin solid line).

Table 3
Chisholm (1973) void fraction correlation, Eq. (23).

	Case A	Case B	Case C
Error	6.34%	7.85%	5.95%

Table 4
Woldesemayat and Ghajar (2007) void fraction correlation, Eq. (25).

	Case A	Case B	Case C
Error	7.31%	10.51%	17.32%

there is no single value of ν that can be used to perform the viscous normalization for the two-phase profile. For comparison, u_τ corresponding to the single-phase simulation is used. In order to plot the liquid viscous sublayer $u_l^+ = y_l^+$ in the same figure, the equation

$$u^+ = y^+ \frac{u_{\tau,l}}{u_\tau} \tag{27}$$

is used, where $u_{\tau,l} = \sqrt{\tau_l/\rho_l}$ is the liquid friction velocity and τ_l is the wall shear stress in the film. Eq. (26) within the gas core of the two-phase flow is plotted using $\kappa = 0.29$ and $c = -3.2$. The location of the interface $h^+ = hu_\tau/\nu$ is also shown. There is clearly a viscous sublayer within the liquid film, as one would expect within a viscously dominated near-wall region. Interestingly, a logarithmic region is observed in Fig. 8(a) within the gas core despite the presence of disperse liquid droplets. The axial, radial, and orthoradial rms velocities appear similar to the single-phase case with maximum values occurring on the gas side of the interface, as shown in Fig. 8(b). The decrease in peak rms relative to the single-phase flow is consistent with the fact that $u_{\tau,\Gamma}/u_\tau = 0.715$, where $u_{\tau,\Gamma} = \sqrt{\tau_\Gamma/\rho_g}$ is the friction velocity at the interface and τ_Γ is the mean interfacial shear stress. In a DNS of a sheared air–water interface, Fulgosi et al. (2003) attribute decreased interfacial friction (relative to a solid wall) to transfer of energy from the flow into form drag as the interface deforms. This idea is consistent with studies that have shown reduced skin friction in turbulent channels when injecting bubbles near walls (Lu et al., 2005; Murai et al., 2007) or by using deformable walls (Kang and Choi, 2000).

We observe that the mean flow of the gas core is qualitatively similar to a single-phase turbulent pipe flow subject to a slip-wall boundary condition. This idea is in agreement with previous numerical results of turbulence near an interface for simplified configurations (Lombardi et al., 1996; Solbakken and Andersson, 2005). Based on such findings, the modified law of the wall for the gas core becomes

$$\frac{u - u_\Gamma}{u_{\tau,\Gamma}} = \frac{(y-h)\,u_{\tau,\Gamma}}{\nu} \tag{28}$$

within the "viscous sublayer", where u_Γ is the mean axial velocity at the interface. We write Eq. (28) compactly as $(u-u_\Gamma)^{+\Gamma} = (y-h)^{+\Gamma}$, and the gas core log law is written as

$$(u-u_\Gamma)^{+\Gamma} = \frac{1}{\kappa}\ln\left[(y-h)^{+\Gamma}\right] + c', \tag{29}$$

where the value of the von Kármán constant $\kappa = 0.35$ for the single-phase log law is recovered, and c' is a constant found to be equal to -2.5. This result is seen in Fig. 9(a) compared with the single-phase profile, plotted as $(u-u_\Gamma)^+ = f((y-h)^+)$ for the sake of comparison. In order to plot the interfacial viscous sublayer in terms of quantities normalized by u_τ, the lower dashed line in Fig. 9(a) is given by the equation

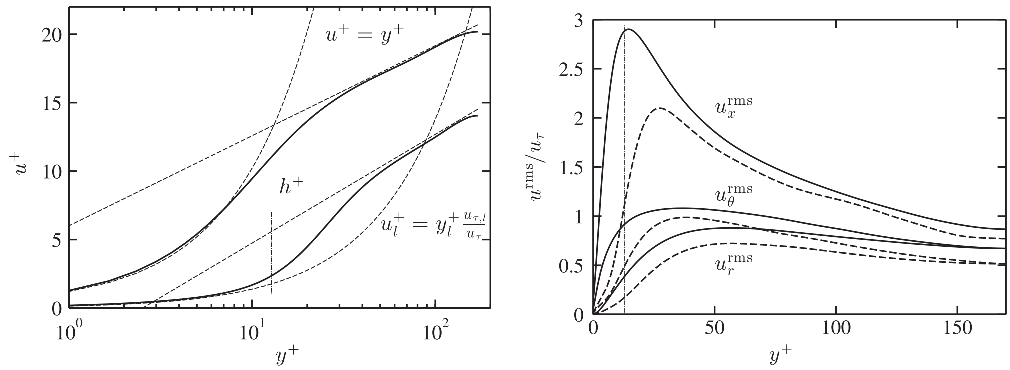

(a) Comparison of the law of the wall for single- (upper solid line) and two-phase (lower solid line) flows. Corresponding viscous sublayers and log law regions are given by the dashed lines, and the dash-dotted vertical line shows the mean h^+

(b) Comparison of the velocity rms for the single- (solid lines) and two-phase (dashed lines) flows. The dash-dotted vertical line shows the mean h^+

Fig. 8. Mean and rms velocities for both case A and the corresponding single-phase flow.

$$(u - u_\Gamma)^+ = \left(\frac{u_{\tau,\Gamma}}{u_\tau}\right)^2 (y - h)^+. \tag{30}$$

The gas core profile follows this narrow interfacial viscous region for $(y-h)^+ \lesssim 2$, and the gas core log law appears to be valid in the region $(y-h)^+ > 30$, which corresponds well with the outer portion of the single-phase buffer region. When plotting the shifted axial velocity rms within the gas core and normalizing by $u_{\tau,\Gamma}$ as in Fig. 9(b), we find that the peak value is roughly equal to the single-phase value normalized by u_τ. It also occurs at roughly the same distance from the interface as does the peak single-phase rms from the wall. Further analysis of annular flows in the form $(u-u_\Gamma)^{+\Gamma} = f((y-h)^{+\Gamma})$ could lead to future modeling efforts built on ideas of existing law of the wall models.

Using liquid properties to normalize by $u_{\tau,l}$ and ν_l, $u_l^+(y_l^+)$ is plotted in Fig. 10, along with the interface location $h_l^+ = 8.83$. The profile deviates from $u_l^+ = y_l^+$ at a value of $y_l^+ \approx 5$ on the liquid side of the interface, indicating that the interface lies outside the near-wall liquid viscous sublayer. This suggests that the outermost region of the liquid film is not completely dominated by viscous affects, which is in agreement with the presence of waves generated through interfacial shear from the turbulent gas core, as is evident in Fig. 3(g). This deviation from laminar behavior in the outermost region of the film will become relevant to the model introduced in ‘A model for the liquid film’.

Profiles of $u^+(y^+)$ at different values of θ are shown in Fig. 11 for cases B and C. Case A is also shown for reference, averaged only about the $\theta = 0$ plane. Similar to case A, viscous sublayers and logarithmic regions are observed for cases B and C. The extent of the regions depends on the θ location, since the film thickness varies with θ. The difference in u^+ from case A is most significant for case C, as the film is much thicker at $\theta/\pi = 0$ than at $\theta/\pi = 1$.

For $\theta/\pi = 0$ and 1/4, it is difficult to tell from Fig. 11(b) if a logarithmic region exists in the gas core. In Fig. 3(i), it is evident that waves protrude far into the gas core due to the increased film thickness near the bottom of the pipe. This protrusion of waves, together with the wall-normal extent of the base film, may prevent the possibility of a logarithmic region for lowers values of θ. A similar argument could be made at $\theta = 0$ for case B, as shown in Fig. 11(a). Modulation of turbulence by a rough interface and slowly moving drops after creation from the film has been shown previously (Azzopardi, 1999), thus it is reasonable to speculate that interfacial motions protruding into the gas core affect the logarithmic region. This is evidenced by the axial velocity rms for cases B

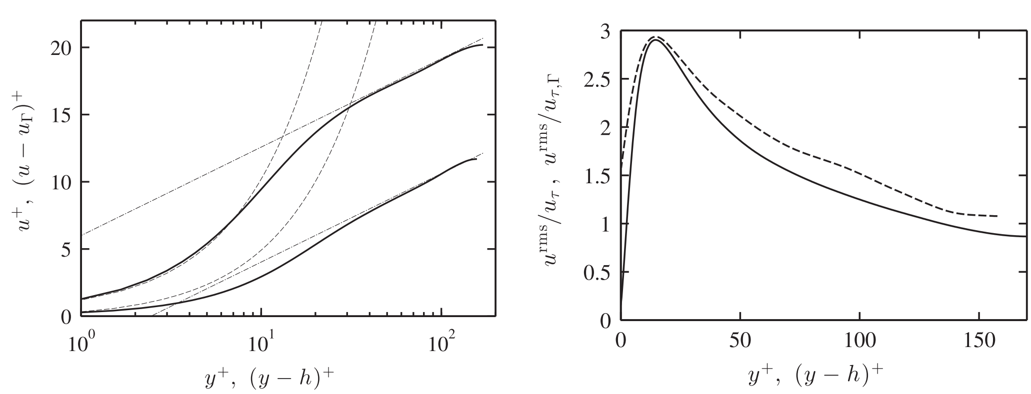

(a) Single-phase law of the wall and modified gas core law of the wall

(b) Single-phase and gas core axial velocity rms

Fig. 9. Comparison between the mean and rms velocities for case A gas core and the single-phase flow. In (a): single-phase profile (upper solid line), shifted gas core profile (lower solid line), single-phase viscous sublayer (upper dashed line), gas core interfacial viscous sublayer (lower dashed line), single-phase log law (upper dash-dotted line), gas core log law (lower dash-dotted line). In (b): single-phase profile (solid line), shifted gas core profile (dashed line).

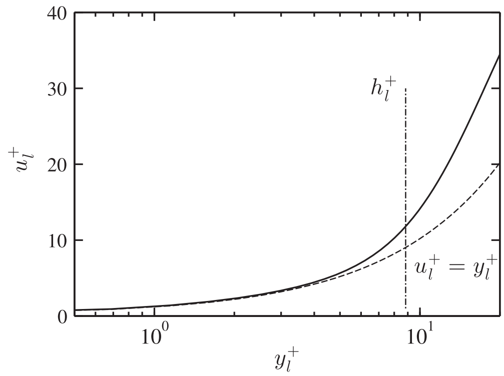

Fig. 10. Velocity profile within the liquid film. $u_l^+(y_l^+)$ (solid line), $u_l^+ = y_l^+$ (dashed line), h_l^+ (dash-dotted line).

and C shown in Fig. 12, which is largest near the interface for low values of θ.

Orthoradial symmetry in case A leads to a clean comparison between radial gas core statistics and the single-phase case. However, the presence of the liquid film imposes a new length scale on the physical system, making the analysis more complicated than the single-phase case. The complexity is further increased for cases B and C, due to mean interfacial shear and film height that are a function of θ. An interesting question is whether or not the asymmetric film effects the radial gas core velocity profile in a qualitatively similar way, regardless of θ. This does seem to be the case, observed by normalizing the shifted gas core profiles by their local $h(\theta)$. The result is shown in Fig. 13, where $(u - u_\Gamma)/u_\tau$ is plotted as a function of $(y - h)/h$. The single-phase log law with $\kappa = 0.35$ and $c = 6$ is shown for comparison. The observed collapse onto a single profile for case B in Fig. 13(a) indicates that the local film height is a good measure of the characteristic viscous length scale for that particular case. Other possible length scales that do not lead to collapse are $\nu_l/u_{\tau,l}$ and $\nu_g/u_{\tau,\Gamma}$. The gas core collapse of case C only seems to work for the three largest θ values in which h does not vary too much. This is reasonable, as the heavily stratified film is likely not dominated by viscous effects near $\theta = 0$. In any case, the idea of collapsing gas core profiles at different θ onto a single profile, assuming $h(\theta)$ does not vary too rapidly, could prove to be useful in future modeling efforts of horizontal annular flows.

Film height and dry-out statistics

The probability of encountering dry-out conditions, i.e., the pipe wall being non-wetted, depends on the average thickness of the liquid film at a particular orthoradial angle. Note that our computational approach does not properly account for the physics at the triple point if the wall becomes non-wetted. The Neumann boundary condition on our level set enforces a 90° contact angle with a solid wall, resulting in a simplified model for contact line dynamics and contact line migration. Although we do not account for proper physics once the wall becomes non-wetted, the present results should provide insight on the onset of dry-out.

As seen in Fig. 14, both case A and case B remain sufficiently wetted for all θ and thus have a zero probability of dry-out. Only symmetry with respect to the $\theta = 0$ plane is exploited for case A for the sake of comparison. The film height $h(\theta)$ is nearly flat for case A and would eventually be perfectly flat if averaged over a

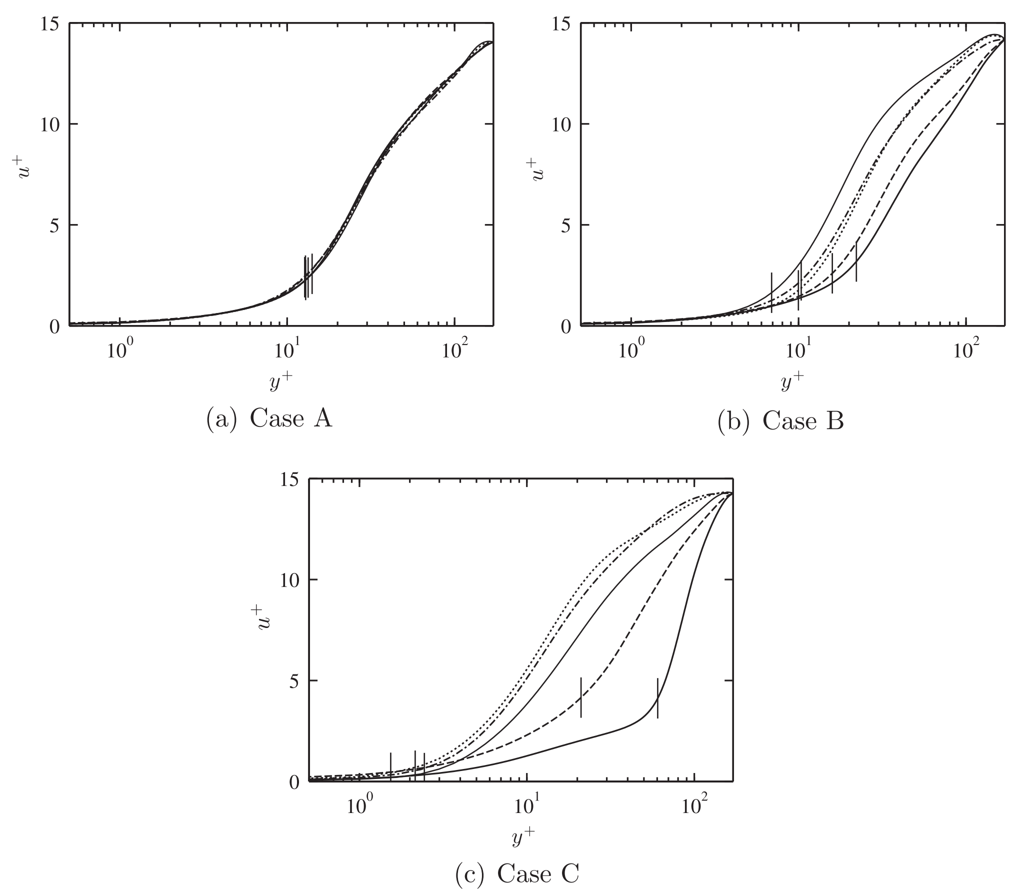

Fig. 11. Mean $u^+(y^+)$ for different values of θ. $\theta/\pi = 0$ (thick solid line), $\theta/\pi = 1/4$ (dashed line), $\theta/\pi = 1/2$ (dash-dotted line), $\theta/\pi = 3/4$ (dotted line), $\theta/\pi = 1$ (thin solid line). The dashed lines give the location of h^+ for each value of θ.

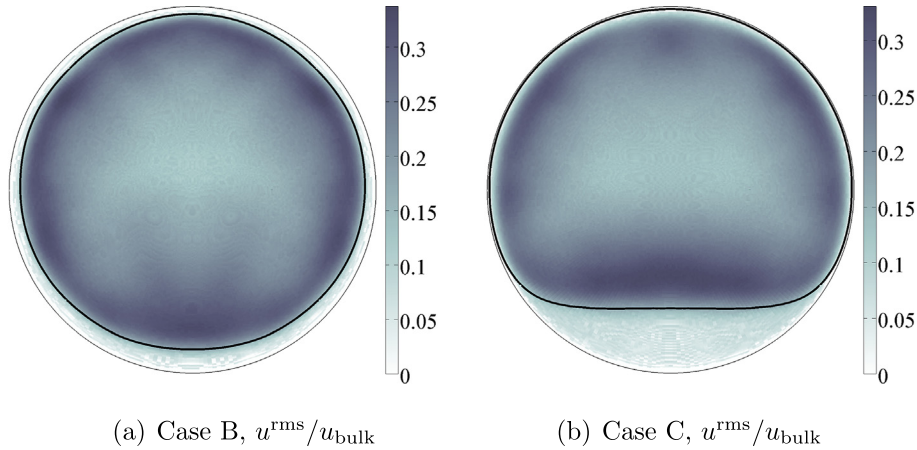

Fig. 12. Axial velocity rms u^{rms} normalized by the bulk axial velocity in case A, u_{bulk}. Values vary from 0 (gray) to $\max(u^{\text{rms}}/u_{\text{bulk}})$ (white), given by the legend. The mean location of the interface $h(\theta)$ is given by the black line.

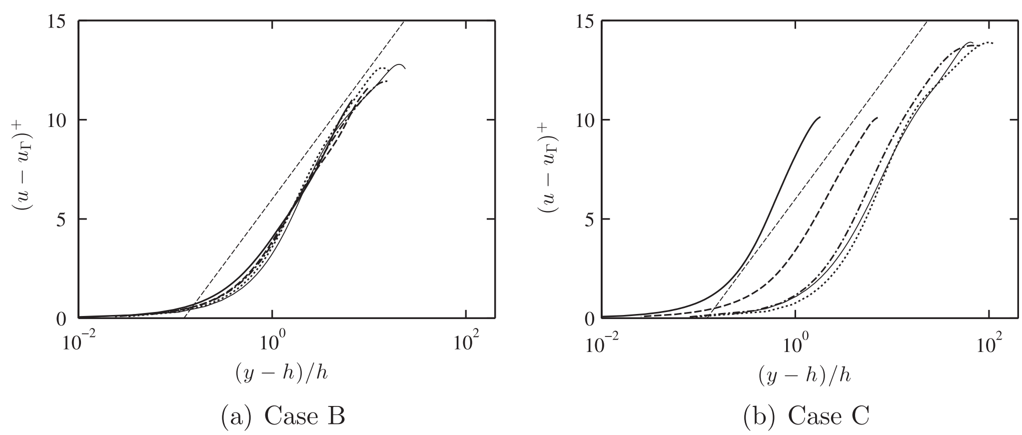

Fig. 13. Collapse of multiple $(u-u_\Gamma)^+((y-h)^+)$ onto $(u-u_\Gamma)^+((y-h)/h)$. $\theta/\pi=0$ (thick solid line), $\theta/\pi=1/4$ (dashed line), $\theta/\pi=1/2$ (dash-dotted line), $\theta/\pi=3/4$ (dotted line), $\theta/\pi=1$ (thin solid line).

long enough period. For case B, h is larger near $\theta=0$ than $\theta=\pi$, as expected. The slight local maximum in $h(\theta)$ near $\theta/\pi\approx 3/4$ could be due to insufficient averaging. For case C, the film thickness is significantly biased toward $\theta=0$ and becomes very thin at the top of the pipe. As a result, P_{dry} varies between 0 and nearly 8% for values of $\theta/\pi>0.4$.

Film thickness calculations from the present simulations are compared to experiments in the literature. Schubring and Shedd (2009b) provide two correlations for the average film thickness $\bar{h}$. In our simulations, we define $\bar{h}$ as

$$\bar{h}=\frac{1}{\pi}\int_0^\pi h(\theta)\,d\theta. \tag{31}$$

In their experiments, Schubring and Shedd (2009b) only measured the film thickness at $\theta/\pi=0$, 1/2, and 1, so Eq. (31) becomes

$$\bar{h}=\frac{1}{4}(h_0+2h_{\pi/2}+h_\pi), \tag{32}$$

where the subscript indicates the value of θ corresponding to h. A simple correlation for $\bar{h}$ provided by Schubring and Shedd (2009b) is

$$\frac{\bar{h}_{\text{corr}}}{D}=12.5\ \text{Re}_g^{-2/3}. \tag{33}$$

They measured the correlation error

$$\text{error}=\frac{|\bar{h}_{\text{corr}}-\bar{h}|}{\bar{h}} \tag{34}$$

for 206 annular data points and reported an average value of 11%. The correlation does not fit the present simulations, as shown in Table 5. The discrepancy is possibly due to high Reynolds and Weber number effects, as most of the experiments were conducted over a range of Re_g and We_g more than an order of magnitude larger than the simulations. Increased inertia could lead to different film characteristics that are not accounted for in this correlation, as well as a higher percentage of liquid taking the form of drops. This would reduce the film height, which is consistent with Eq. (33) underpredicting the simulation mean film height for all three cases.

The previous correlation is based entirely on the gas phase. In order to account for the presence of the liquid film, Schubring and Shedd (2009b) also proposed

$$\frac{\bar{h}_{\text{corr}}}{D}=4.7\,\frac{1}{x}\left(\frac{\rho_g}{\rho_l}\right)^{1/3}\text{Re}_g^{-2/3}, \tag{35}$$

where

$$\text{Re}_G=\frac{GD}{\mu_l} \tag{36}$$

is a Reynolds number based on the mass velocity and liquid viscosity. We find that the inclusion of liquid film processes causes the correlation to fit better with the current simulations than the previous one, as seen in Table 6. Note that the improvement is only observed for cases A and B, which is reasonable, since they fall within the annular regime that Eq. (35) is based on. The experimental

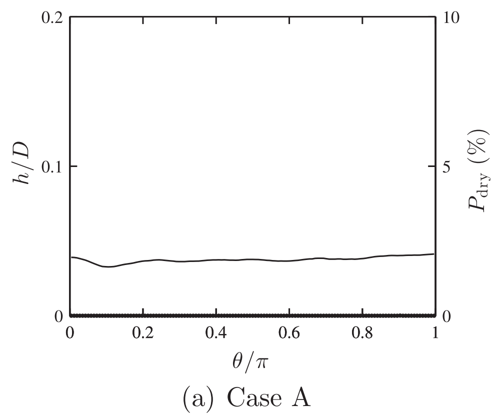

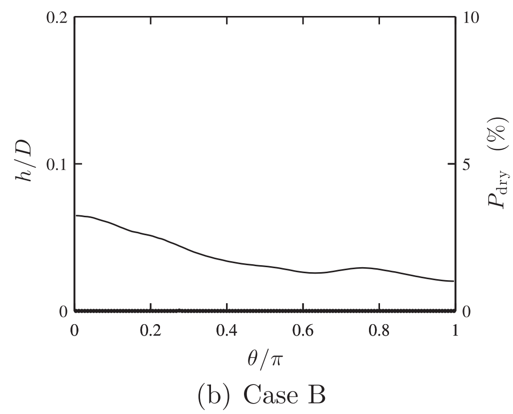

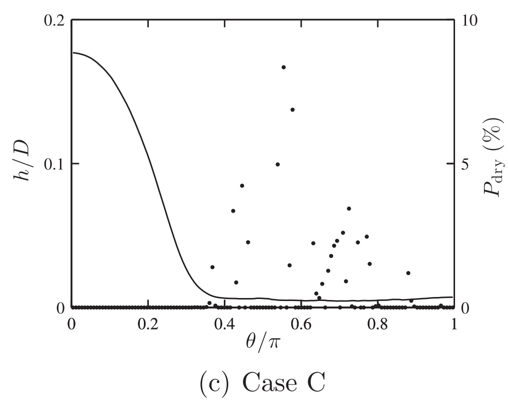

Fig. 14. Mean film thickness $h(\theta)$ and dry-out probability $P_{\mathrm{dry}}(\theta)$ for the three cases. $h(\theta)$ (solid line), $P_{\mathrm{dry}}(\theta)$ (•).

Table 5
Film height correlation error (computed from Eq. (34)) when compared to Eq. (33) (Schubring and Shedd, 2009b).

	Case A	Case B	Case C
Error	48.77%	49.69%	26.18%

film heights from the data bank of Schubring and Shedd (2009b) have been normalized by pipe diameter in order to compare them with the present simulations, as shown in Fig. 15. Good agreement relative to the spread of the experimental data is observed.

In addition to the mean film thickness, Schubring and Shedd (2009b) also provide a correlation for the asymmetry of the liquid film, defined as

$$\mathcal{A} = \frac{h_0}{h_\pi}. \tag{37}$$

The correlation is

$$\mathcal{A}_{\mathrm{corr}} = \left(1 - e^{-0.63\mathrm{Fr}_h}\right)^{-1}, \tag{38}$$

where

$$\mathrm{Fr}_h = \frac{\rho_g j_g}{\rho_l (g\bar{h})^{1/2}} \tag{39}$$

Table 6
Film height correlation error (computed from Eq. (34)) when compared to Eq. (35) (Schubring and Shedd, 2009b).

	Case A	Case B	Case C
Error	21.16%	22.49%	32.95%

is a Froude number based on the superficial gas velocity and the mean film thickness. Asymmetry for case A is unity, since $\mathrm{Fr}_g = \infty$ and $h_0 = h_\pi$. Eq. (39) significantly overpredicts asymmetry for cases B and C, and the errors $|\mathcal{A}_{\mathrm{corr}} - \mathcal{A}|/\mathcal{A}$ are shown in Table 7. Eq. (38) is based on annular experiments with $g = 9.81\ \mathrm{m/s^2}$ and may therefore encompass physical processes not present in the simulations. Also, Eq. (38) is based on experiments with $\mathcal{A} < 3.5$, and thus may not incorporate physical processes for heavily stratified films.

A more detailed asymmetry correlation is provided by Hurlburt and Newell (2000), which accounts for asymmetry by defining

$$\widetilde{\mathcal{A}} = \frac{\bar{h}}{h_0}, \tag{40}$$

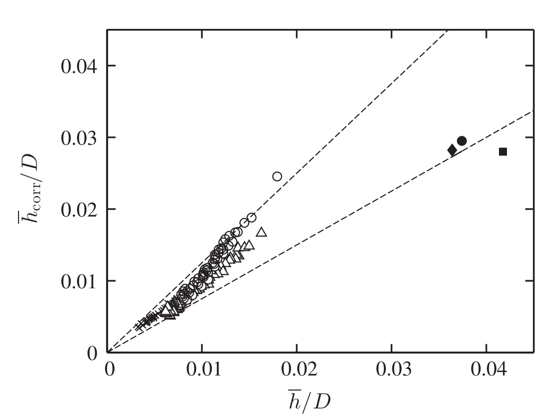

Fig. 15. Film height correlation of Schubring and Shedd (2009b), Eq. (35). Case A (•), case B (◆), case C (■), ±25% (dashed lines). Open symbols denote different pipe diameters from the experiments: 8.8 mm (○), 15.1 mm (△), 26.3 mm (×).

where $\bar{h}$ is defined by Eq. (31). Fig. 16 shows $\widetilde{\mathcal{A}}$ as a function of $(\dot{m}_g/\dot{m}_l)^{1/2}\mathrm{Fr}_{sg}$ for all three cases, compared to a wide range of experimental data. The curve fit to the data in Fig. 16 is given as

$$\widetilde{\mathcal{A}} = \frac{4}{3\pi}\left(\frac{\bar{h}_0}{D}\right)^{1/2} + 0.9\left(1 - \exp\left(\frac{-(\dot{m}_g/\dot{m}_l)^{1/2}\,\mathrm{Fr}_{sg}}{90}\right)\right), \qquad (41)$$

where $\bar{h}_0$ is a value of h_o representative of the data, and $\mathrm{Fr}_{sg} = j_g/(gD)^{1/2}$ is a Froude number based on the superficial gas velocity and pipe diameter. Specifying $\bar{h}_0$ as the mean h_0 of the experimental data leads to the solid line in Fig. 16, while using the mean h_0 of the simulations as $\bar{h}_0$ leads to the dashed line. Either way, $\widetilde{\mathcal{A}}$ from the simulations agrees well with Eq. (41) with respect to the spread of the experimental data. Note that the abscissa of Fig. 16 is ∞ for case A, and the value of $\widetilde{\mathcal{A}} = 1$ is shown at the right of the figure (with an arrow pointing to the right) for the sake of comparison.

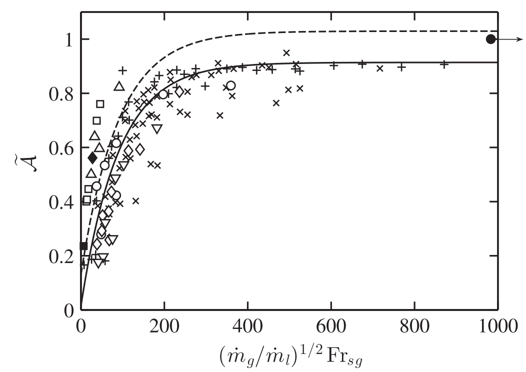

Fig. 16. Film asymmetry $\widetilde{\mathcal{A}}$ compared to experimental data. Eq. (41) with $\bar{h}_0$ as the mean h_0 of the experiments (solid line) and as the mean of the simulations (dashed line). Case A (●), case B (◆), case C (■), Dallman (1978) (×), Fukano and Ousaka (1989) (○), Hurlburt and Newell (1996) (△), Jayanti et al. (1990a) (□), Laurinat and Hanratty (1982) (+), Paras and Karabelas (1991a) (◇), Williams (1990) (▽).

Dynamics in the pipe cross section

In the absence of mechanisms for replenishing the liquid film near $\theta/\pi = 1$, all of the liquid would drain due to gravity and the flow would become stratified. Much debate has centered around the mechanisms for film sustainment, possible explanations being that drops are entrained near lower values of θ and deposited near higher values (Russell and Lamb, 1965), the action of surface waves moves liquid in the circumferential direction (Butterworth, 1968; Butterworth, 1972; Fukano and Inatomi, 2003; Fukano and Ousaka, 1989; Jayanti et al., 1990b; Sutharshan et al., 1995), and circumferential variations in interfacial roughness cause secondary gas flows which slow film drainage due to gravity (Butterworth, 1972; Darling and McManus, 1968; Flores et al., 1995; Laurinat et al., 1985; Lin et al., 1985). While it is not the goal of this work to offer a definitive explanation for liquid film sustainment, the statistics reported here do provide some insight toward understanding this phenomenon.

Cross-sectional liquid motion

In the present study, a band-growth algorithm was used to separate the liquid in the simulation domain into contiguous regions. This allows us to separate the droplets from the base film and track their displacement in time in order to compute droplet velocities, analogous to particle image velocimetry (PIV). The algorithm was originally developed by Herrmann (2010) for tracking droplets during primary atomization and has been applied to bubble tracking in dense fluidized beds (Pepiot and Desjardins, 2012; Capecelatro and Desjardins, 2013; Capecelatro et al., 2014). Isolating droplets from the base film allows us to compute their contribution to the total liquid volume. Defining the operator $\langle * \rangle_i$ as an average with respect to coordinate i, Table 8 shows the temporal mean of the ratio of liquid droplet volume V_l^d to total liquid volume V_l for the three cases, and it is clear that the amount of liquid in the form of drops decreases as Fr_g increases. It follows naturally that axial mass transport of liquid in the form of drops, denoted by $\dot{m}_l^d$, also decreases with increasing Fr_g, as shown by the mean ratio of $\dot{m}_l^d$ to the total liquid flow rate in Table 8. This is in keeping with qualitative analysis of Fig. 3 as well as previous experimental results (Simmons and Hanratty, 2001), which suggest that increased stratification leads to significantly fewer disperse drops within the gas core.

We use the orthoradial phase-averaged liquid velocity to examine the liquid motion in the pipe cross section, defined as

$$\boldsymbol{u}_l(r,\theta) = \frac{\langle \alpha_l(\boldsymbol{x},t)\,\boldsymbol{u}_{r\theta}(\boldsymbol{x},t)\rangle_{x,t}}{\langle \alpha_l(\boldsymbol{x},t)\rangle_{x,t}}. \qquad (42)$$

Vectors of $\boldsymbol{u}_l$ in the $r-\theta$ cross-section for cases B and C are shown in Fig. 17, normalized by u_l, the bulk axial liquid velocity for case A. We compute $\boldsymbol{u}_l$ for $\langle\alpha_l\rangle_{x,t} > 0.05$ in order to obtain clean statistics, since converged drop statistics in the gas core require longer run times than are tractable in the present study. Relative to the mean film height, the direction of the arrows for case B in Fig. 17(a) indicates that the film is predominantly draining on the wall side of the mean interface location. Just across the mean interface on the gas side, however, there is clearly flow of liquid in the positive θ direction until $\theta \approx \pi/2$, indicating the circumferential propagation of waves that protrude into the gas core to a height larger than the mean film height. The termination of this wave propagation near $\theta \approx \pi/2$ suggests that wave pumping is not solely responsible for transporting liquid to the top of the pipe. Given that 26% of the liquid flux through the cross section is in the form of drops, it is possible that drop deposition could account for sustainment in upper regions of the pipe.

The scenario is very different for the heavily stratified film of case C shown in Fig. 17(b), which depicts circumferential motion of liquid until $\theta \approx \pi/4$, before the flow returns along the wall toward $\theta = 0$. The flows within the film from the opposite sides of the pipe meet at $\theta = 0$ and are forced to the surface, leading to the establishment of a counter-rotating vortex pair (CVP). In qualitative agreement with Fig. 3(i), negligible transport of liquid in the form of drops indicates that droplets do not act to replenish the film.

Table 7
Error of Schubring and Shedd (2009b) film asymmetry correlation (Eq. (35)) for the simulations.

	Case A	Case B	Case C
Error	0%	68.09%	93.30%

Table 8
Ratio of liquid drop volume to total liquid volume and ratio of axial drop flow rate to total liquid flow rate.

Case	Fr_g	$\langle V_l^d/V_l\rangle_t$	$\langle \dot{m}_l^d/\dot{m}_l\rangle_t$
A	∞	0.063	0.37
B	4.56	0.039	0.26
C	1.20	0.0005	0.0024

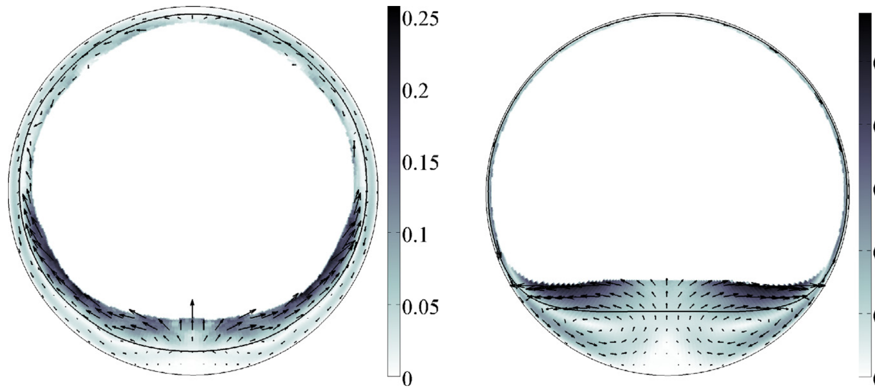

(a) Case B, $\boldsymbol{u}_l/u_l$ (b) Case C, $\boldsymbol{u}_l/u_l$

Fig. 17. Liquid motion in the r–θ plane. Arrows indicate direction and the color palettes give magnitude. The solid black line shows the mean location of the interface. (a) and (c) are normalized by the bulk axial liquid velocity for case A, u_l. (For interpretation of the references to color in this figure legend, the reader is referred to the web version of this article.)

Cross-sectional gas motion

The idea that circumferential variations in pipe surface roughness induce orthoradial circulation was initially proposed in the experimental work of Darling and McManus (1968), and this mechanism is believed to be relevant to horizontal annular flows due to the increased waviness of the interface in lower regions of the pipe relative to upper regions. Numerical simulations of Jayanti et al. (1990b) showed secondary gas flows by using wall functions to represent differential wall roughness, and possible streamlines of secondary flows in horizontal annular flows were proposed based on the experiments of Jayanti et al. (1990a). Later on, the experiments of Flores et al. (1995) confirmed the existence of secondary gas flows in an air–water annular flow. Recently, van't Westende et al. (2007) performed large-eddy simulations to study the effects of gravitational settling, turbophoresis, and secondary gas flows on droplets by modeling the film as a wall with circumferentially varying roughness and modeling the droplets as solid spheres. Their conclusion regarding secondary flows was that gas circulation alters deposition of the droplets, and secondary flow centrifugal effects can lead to increased deposition in regions of high orthoradial gas velocity. Secondary gas flows induced by θ variations in interfacial topology are physically constrained to maintain a net-zero circulation, explaining the CVP that has been observed (Jayanti et al., 1990b; van't Westende et al., 2007).

We write the phase-averaged gas velocity in the cross section as

$$\boldsymbol{u}_g(r,\theta) = \frac{\langle \alpha_g(\boldsymbol{x},t)\,\boldsymbol{u}_{r\theta}(\boldsymbol{x},t)\rangle_{x,t}}{\langle \alpha_g(\boldsymbol{x},t)\rangle_{x,t}}. \tag{43}$$

Fig. 18 shows $\boldsymbol{u}_g$ for cases B and C, normalized by u_g, the bulk axial gas phase-averaged velocity for case A. A CVP is clearly present within the gas core. The strength of the vortices for case C relative to case B lead to a more clearly defined vortex center, likely due to the absence of disperse droplets. Bringing the gas phase vortices together with the motion of liquid film in Fig. 17 leads to oppositely signed circulation within each quadrant of the pipe when the average velocity in the r–θ plane is computed, defined as

$$\bar{\boldsymbol{u}}(r,\theta) = \langle \boldsymbol{u}_{r\theta}(\boldsymbol{x},t)\rangle_{x,t}. \tag{44}$$

Fig. 19 shows streamlines of $\bar{\boldsymbol{u}}$ and their magnitude. Vortices in the stratified film appear much more coherent for case C than for case B. This is due to the increased film thickness and faster gas circulation speed, which is nearly 10% of u_{bulk}, compared to less than 4% for case B.

Fig. 20 shows the θ component of $\bar{\boldsymbol{u}}$ as a function of y/R and θ/π for cases B and C. Fig. 20(a) shows that $\bar{u}_\theta < 0$ for $y < h$, then $\bar{u}_\theta$ increases to a local maximum on the gas side of the interface. Essentially the same behavior is observed for case C, as shown in Fig. 20(b).

A model for the liquid film

The concepts of secondary gas flows and wave pumping lead to a simple model that aids in characterizing the behavior of the liquid film. Assuming the mean film thickness h is small compared to the radius of curvature of the pipe, the (y,θ) polar coordinates (recall that $y = R - r$) are approximated by a local Cartesian coordinate system, i.e., $(y,\theta) \to (\mathcal{Y},\mathcal{X})$, where $\mathcal{X}$ is the wall-parallel coordinate and $\mathcal{Y}$ is the wall-normal coordinate, as shown in Fig. 21. In the model, the liquid film is characterized by gravitational acceleration and shear at the interface location h, due to the θ component of the secondary gas flow $\bar{u}_\theta$. Assuming that the velocity profile across the liquid film is laminar, is in the $\mathcal{X}$-direction, and varies only with $\mathcal{Y}$, the momentum equation in the simplified coordinate system gives

$$\frac{\partial^2 u_{\mathcal{X}}}{\partial \mathcal{Y}^2} = \frac{g_{\mathcal{X}}}{\nu_l} + \frac{1}{\mu_l}\frac{\partial p}{\partial \mathcal{X}}, \tag{45}$$

where $g_{\mathcal{X}}$ is the component of gravity in the negative $\mathcal{X}$-direction, and $\partial p/\partial \mathcal{X}$ is the pressure gradient in the $\mathcal{X}$-direction. The boundary conditions satisfied by $u_{\mathcal{X}}(\mathcal{Y})$ are

$$\begin{aligned} &u_{\mathcal{X}}(\mathcal{Y}=0) = 0 \\ &u_{\mathcal{X}}(\mathcal{Y}=h) = \bar{u}_\theta(y=h) = u_{\theta,\Gamma}. \end{aligned} \tag{46}$$

Utilizing these boundary conditions and acknowledging that $g_{\mathcal{X}} = g\sin\theta$, the velocity across the film is given as

$$u_{\mathcal{X}}(\mathcal{Y}) = \frac{u_{\theta,\Gamma}}{h}\mathcal{Y} + \frac{1}{2}\left(\frac{g\sin\theta}{\nu} + \frac{1}{\mu_l}\frac{\partial p}{\partial \mathcal{X}}\right)(\mathcal{Y}^2 - \mathcal{Y}h). \tag{47}$$

Although the circumferential pressure gradient could be computed from the simulation, the value of $\partial p/\partial \mathcal{X}$ provided to Eq. (47) is optimized in order to minimize $|\langle \bar{u}_\theta\rangle_h - \langle u_{\mathcal{X}}\rangle_h|$, where the operator

$$\langle (*)\rangle_h = \frac{1}{h}\int_0^h (*)\,\mathrm{d}y \tag{48}$$

has been used to denote a film-averaged quantity, and $\langle \bar{u}_\theta\rangle_h$ and $\langle u_{\mathcal{X}}\rangle_h$ are the bulk velocities within the film for the simulation and the model, respectively. The resulting values of $(\partial p/\partial \mathcal{X})/f_b$ vary

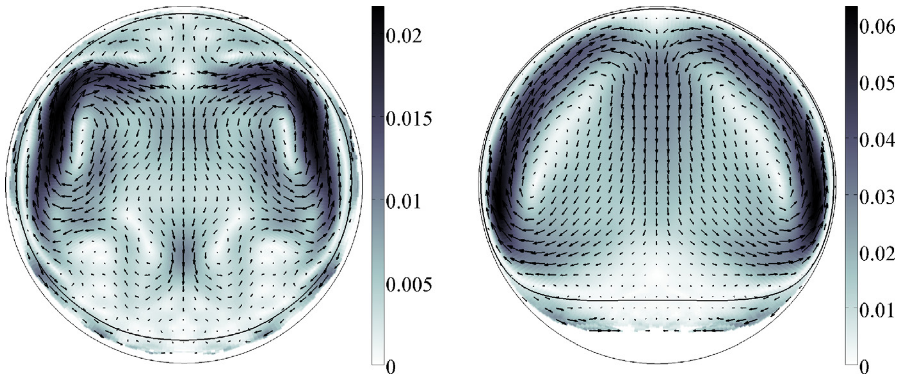

(a) Case B, $\boldsymbol{u}_g/u_g$ (b) Case C, $\boldsymbol{u}_g/u_g$

Fig. 18. Gas motion in the $r-\theta$ plane. Arrows indicate direction and the color palettes give magnitude. The solid black line shows the mean location of the interface. $\boldsymbol{u}_g$ is normalized by the bulk axial gas velocity for case A, u_g. (For interpretation of the references to color in this figure legend, the reader is referred to the web version of this article.)

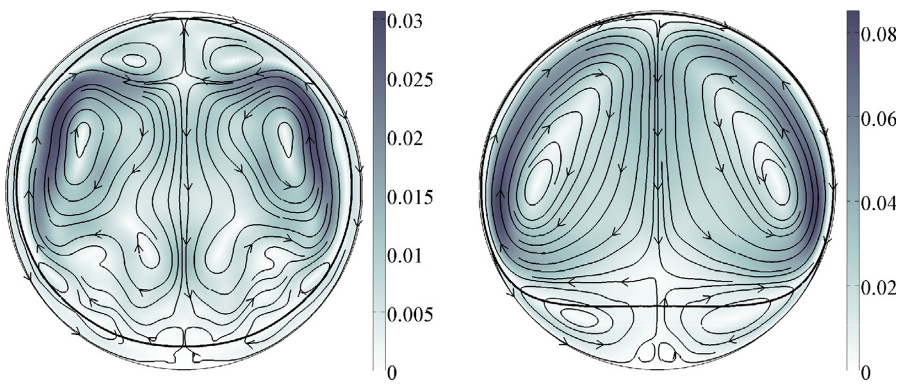

(a) Case B, $\overline{\boldsymbol{u}}/u_{\text{bulk}}$ (b) Case C, $\overline{\boldsymbol{u}}/u_{\text{bulk}}$

Fig. 19. Mean cross-sectional velocity $\bar{\boldsymbol{u}}(r,\theta)$ normalized by u_{bulk}, the bulk axial velocity for case A. The thick black line shows the mean location of the interface, color palettes give velocity magnitude, and thin black lines with arrows show streamlines. (For interpretation of the references to color in this figure legend, the reader is referred to the web version of this article.)

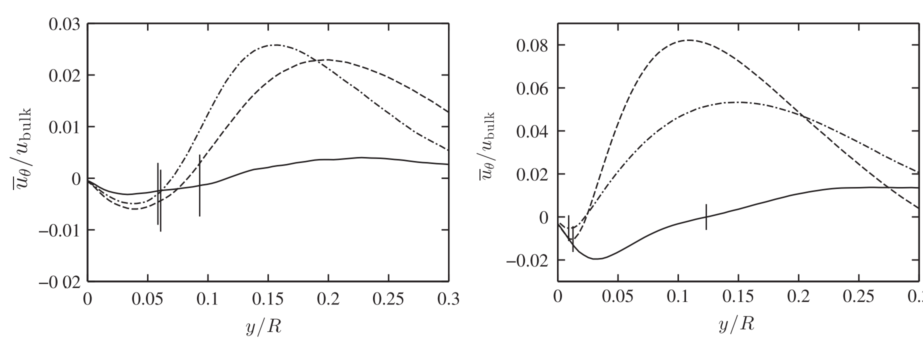

(a) Case B (b) Case C

Fig. 20. $\bar{u}_\theta$ Normalized by u_{bulk} (the bulk axial velocity for case A) as a function of y/R : $\theta/\pi = 1/4$ (solid line), $\theta/\pi = 1/2$ (dashed line), $\theta/\pi = 3/4$ (dash-dotted line), $h(\theta)/R$ (vertical lines).

within 30–70% (recall that f_b is the axial source term described in 'Flow forcing').

Fig. 22 compares the model velocity $u_{\mathcal{X}}$ with the computed θ velocity $\bar{u}_\theta$ at different values of θ for case B. The orthoradial velocity is well-approximated by the simple model inside the liquid film, which is the intended goal. Table 9 gives the L_2 error of the velocity profile between the model and simulation within the region $0 < \mathcal{Y} < h$ for each value of θ. Low values of the L_2 profile error indicate that the orthoradial velocity in the film is well-approximated by a laminar parabolic profile.

An important conclusion is that the bulk velocity of the film in the $\mathcal{X}$-direction is negative for all values of θ. This implies that interfacial shear induced by secondary gas flow is not strong enough to overcome gravitational draining of the film, an argument supported by previous findings (Jayanti et al., 1990b). This is further elucidated by using Eqs. (47) and (48) to write out $\langle u_{\mathcal{X}} \rangle_h$, which yields

$$\langle u_{\mathcal{X}} \rangle_h = \frac{u_{\theta,\Gamma}}{2} - \frac{h^2}{12}\left(\frac{g\sin\theta}{\nu_l} + \frac{1}{\mu_l}\frac{\partial p}{\partial \mathcal{X}}\right). \tag{49}$$

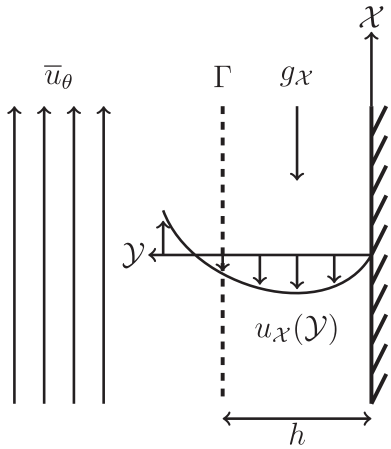

Fig. 21. Schematic of the liquid film model.

This implies that $\langle u_\mathcal{X}\rangle_h > 0$ if the condition

$$u_{\theta,\Gamma} > \frac{h^2}{6}\left(\frac{g\sin\theta}{\nu_l} + \frac{1}{\mu_l}\frac{\partial p}{\partial \mathcal{X}}\right) \tag{50}$$

is satisfied. Since $\sin\theta > 0$ for $0 < \theta < \pi$, $\partial p/\partial\mathcal{X}$ is positive for all θ in the model, and $u_{\theta,\Gamma} < 0$ in Fig. 22, this cannot occur. However, the fact that the bulk film velocity is largest at the minimum value of θ is in keeping with Eq. (50). This further strengthens the idea that secondary flows can slow down gravitational drainage through shear, but the shear is not strong enough to move liquid up the wall. Essentially the same conclusion is drawn when applying the model to case C, but the lack of resolution in the liquid film for large θ due to heavy stratification makes the analysis less informative, and it is therefore not shown.

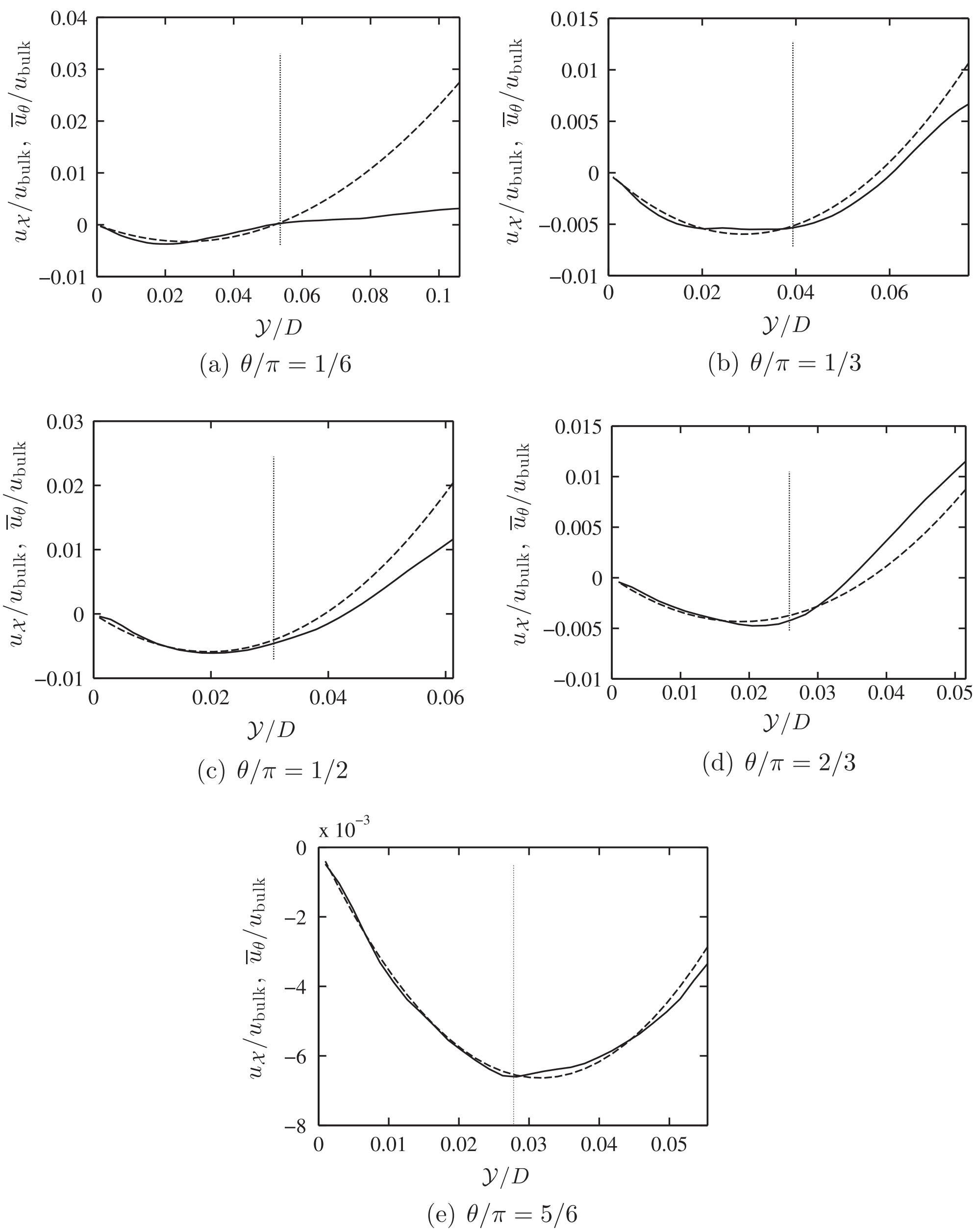

Fig. 22. Comparison between computed velocity $\bar{u}_\theta$ (solid line) and model velocity $u_\mathcal{X}$, with ν_t computed from the mixing length (dashed line) and by minimizing $|\langle\bar{u}_\theta\rangle_h - \langle u_\mathcal{X}\rangle_h|$ (dash-dotted line). The location of the interface is shown by the vertical dotted line.

Table 9
L_2 Profile error between the simulation and the model.

θ	L_2 Error
$\pi/6$	9.195×10^{-5}
$\pi/3$	4.983×10^{-5}
$\pi/2$	4.697×10^{-5}
$2\pi/3$	3.691×10^{-5}
$5\pi/6$	1.188×10^{-5}

Conclusion

In this work a general strategy for numerical simulation of liquid–gas annular pipe flows is outlined. A turbulent gas core, a fully deformable phase interface, and non-unity density and viscosity ratios are all accounted for, allowing for an original numerical exploration of gravitational effects in horizontal liquid–gas flows from first principles. We provide descriptions of the phase interface capture scheme, the immersed boundary method used to represent the enclosing pipe, and the mechanism used to force the two-phase flow. The mesh and immersed boundary used in the two-phase simulations are validated against a corresponding single-phase turbulent pipe flow, showing excellent agreement for both first and second order velocity statistics.

Governing parameters of the system are shown through dimensional analysis and used to characterize the global behavior of three simulations with increasing importance of gravitational effects relative to inertial effects. By increasing the Froude number through numerically decreasing gravitational acceleration, simulations within the annular and stratified-annular regime are performed. Results indicate that the present approach is capable of capturing the transition between these regimes, which was a principal directive of this exploratory study.

Detailed statistics of the flows are provided, including how stratification of liquid droplets and the base film modifies liquid volume fraction and axial velocity profiles and increases the probability of encountering dry-out conditions. Modification to the turbulent law of the wall by the liquid film is investigated, and it is seen that a viscous sublayer is observed within the liquid film, and both viscous and logarithmic regions exist within the gas core. The void fraction, liquid film height, and film asymmetry in the simulations are all shown to agree within reason with experimental data and correlations.

Statistical flow features within the pipe cross section are analyzed, and results suggest that, for the case in which the film is not significantly drained, the action of surface waves drives liquid roughly halfway up the pipe walls. Droplets account for nearly 30% of liquid transport for this case, compared to less than 1% for the heavily stratified case, leading to the possibility that preferential droplet deposition could play a role in film replenishment in upper regions of the pipe. Secondary gas flows are observed within the pipe cross section, likely induced by circumferential gradients in interfacial roughness. Shearing of the liquid film imposed by secondary gas flow acts to slow the gravitational drainage of the film, an idea that is further substantiated by a simple model for the film.

Previous computations have been performed that simulate simplified aspects of a horizontal liquid–gas annular flow, such as modeling the base film through wall roughness functions, modeling entrained droplets with solid particles, or detailed simulation of a sheared phase interface. This exploratory study demonstrates that it is feasible to perform simulations that combine the majority of the physical processes that occur in realistic annular flows and capture global features like flow regime transition. The hope of this work is to promote future similar studies, as much can be learned from a direct simulation approach that may not be attained through reduced order models or experimental correlation and observation alone.

Acknowledgements

This work is funded in part by Abengoa Research, Contract No. OCG 5478 B. Support from the National Institute for Computational Sciences, made possible through an NSF TeraGrid allocation, is gratefully acknowledged.

References

Adechy, D., 2004. Modelling of annular flow through pipes and T-junctions. Comput. Fluids 33 (2), 289–313.
Alekseenko, S., Cherdantsev, A., Markovich, D., Rabusov, A., 2013. Dynamics of heavy droplets and large bubbles in annular gas–liquid flow. In: 8th International Conference on Multiphase Flow, Jeju, Korea, pp. 1–8.
Al-Sarkhi, A., Hanratty, T., 2002. Effect of pipe diameter on the drop size in a horizontal annular gas–liquid flow. Int. J. Multiphase Flow 28 (10), 1617–1629.
Al-Sarkhi, A., Sarica, C., Qureshi, B., 2012. Modeling of droplet entrainment in co-current annular two-phase flow: a new approach. Int. J. Multiphase Flow 39, 21–28.
Alves, G., 1954. Cocurrent liquid–gas flow in a pipe-line contactor. Chem. Eng. Prog. 50 (9), 449–456.
Anderson, R.J., Russel, T.W.F., 1970. Circumferential variation of interchange in horizontal annular two-phase flow. Ind. Eng. Chem. Fundam. 9 (3), 340–344.
Azzopardi, B., 1999. Turbulence modification in annular gas/liquid flow. Int. J. Multiphase Flow 25 (6-7), 945–955.
Baker, O., 1953. Design of pipelines for the simultaneous flow of oil and gas. In: Fall Meeting of the Petroleum Branch of AIME.
Bonizzi, M., Issa, R., 2003a. On the simulation of three-phase slug flow in nearly horizontal pipes using the multi-fluid model. Int. J. Multiphase Flow 29 (11), 1719–1747.
Bonizzi, M., Issa, R., 2003b. A model for simulating gas bubble entrainment in two-phase horizontal slug flow. Int. J. Multiphase Flow 29 (11), 1685–1717.
Bunner, B., Tryggvason, G., 1999. Direct numerical simulations of three-dimensional bubbly flows. Phys. Fluids 11 (8), 1967–1969.
Bunner, B., Tryggvason, G., 2002a. Dynamics of homogeneous bubbly flows – Part 1: Rise velocity and microstructure of the bubbles. J. Fluid Mech. 466, 17–52.
Bunner, B., Tryggvason, G., 2002b. Dynamics of homogeneous bubbly flows – Part 2: Velocity fluctuations. J. Fluid Mech. 466, 53–84.
Butterworth, D., 1968. Air–water climbing film flow in an eccentric annulus. In: Int. Symposium on Research on C-Current Gas–Liquid Flow, Waterloo, Ontario, pp. 145–201.
Butterworth, D., 1972. Air–water annular flow in a horizontal tube. Prog. Heat Mass Transfer 6, 235–251.
Butterworth, D., 1975. A comparison of some void-fraction relationships for co-current gas–liquid flow. Int. J. Multiphase Flow 1 (6), 845–850.
Capecelatro, J., Desjardins, O., 2013. An Euler–Lagrange strategy for simulating particle-laden flows. J. Comput. Phys. 238, 1–31.
Capecelatro, J., Pepiot, P., Desjardins, O., 2014. Numerical characterization and modeling of particle clustering in wall-bounded vertical risers. Chem. Eng. J. 245, 295–310.
Carey, V.P., 2008. Liquid–Vapor Phase-Change Phenomena: An Introduction to the Thermophysics of Vaporization and Condensation Processes in Heat Transfer Equipment. Taylor & Francis Group.
Chisholm, D., 1973. Pressure gradients due to friction during the flow of evaporating two-phase mixtures in smooth tubes and channels. Int. J. Heat Mass Transfer 16 (2), 347–358.
Coddington, P., Macian, R., 2002. A study of the performance of void fraction correlations used in the context of drift-flux two-phase flow models. Nucl. Eng. Des. 215 (3), 199–216.
Dallman, J.C., 1978. Investigation of Separated Flow Model in Annular Gas–Liquid Two-Phase Flows. Ph.D. Thesis, University of Illinois, Urbana.
Darling, R., McManus, H., 1968. Flow patterns in circular ducts with circumferential variation of roughness: a two-phase flow analog. In: Proceedings of the 11th Midwestern Mechanics Conference, vol. 5, pp. 153–170.
Desjardins, O., Blanquart, G., Balarac, G., Pitsch, H., 2008a. High order conservative finite difference scheme for variable density low Mach number turbulent flows. J. Comput. Phys. 227 (15), 7125–7159.
Desjardins, O., Moureau, V., Pitsch, H., 2008b. An accurate conservative level set/ghost fluid method for simulating turbulent atomization. J. Comput. Phys. 227 (18), 8395–8416.
Desjardins, O., McCaslin, J.O., Owkes, M., Brady, P., 2013. Direct numerical and large-eddy simulation of primary atomization in complex geometries. Atomizat. Sprays 23 (11), 1001–1048.
Esmaeeli, A., Tryggvason, G., 1998. Direct numerical simulations of bubbly flows – Part 1: Low Reynolds number arrays. J. Fluid Mech. 377, 313–345.
Esmaeeli, A., Tryggvason, G., 1999. Direct numerical simulations of bubbly flows – Part 2: Moderate Reynolds number arrays. J. Fluid Mech. 385, 325–358.

Farias, P.S.C. Martins, F.J.W.a., Sampaio, L.E.B., Serfaty, R., Azevedo, L.F.a. Liquid film characterization in horizontal, annular, two-phase, gas–liquid flow using time-resolved laser-induced fluorescence. Exp. Fluids.
Fedkiw, R.P., Aslam, T.D., Merriman, B., Osher, S., 1999. A non-oscillatory Eulerian approach to interfaces in multimaterial flows (the ghost fluid method). J. Comput. Phys. 152 (2), 457–492.
Flores, A.G., Crowe, K.E., Griffith, P., 1995. Gas-phase secondary flow in horizontal, stratified and annular two-phase flow. Int. J. Multiphase Flow 21 (2), 207–221.
Fukagata, K., Kasagi, N., 2002. Highly energy-conservative finite difference method for the cylindrical coordinate system. J. Comput. Phys. 181 (2), 478–498.
Fukano, T., Inatomi, T., 2003. Analysis of liquid film formation in a horizontal annular flow by DNS. Int. J. Multiphase Flow 29 (9), 1413–1430.
Fukano, T., Ousaka, A., 1989. Prediction of the circumferential distribution of film thickness in horizontal and near-horizontal gas–liquid annular flows. Int. J. Multiphase Flow 15 (3), 403–419.
Fulgosi, M., Lakehal, D., Banerjee, S., De Angelis, V., 2003. Direct numerical simulation of turbulence in a sheared air–water flow with a deformable interface. J. Fluid Mech. 482, 319–345.
Ghajar, A.J., Tang, C.C., 2007. Heat transfer measurements, flow pattern maps, and flow visualization for non-boiling two-phase flow in horizontal and slightly inclined pipe. Heat Transfer Eng. 28 (6), 525–540.
Hagiwara, Y., Esmaeilzadeh, E., Tsutsui, H., Suzuki, K., 1989. Simultaneous measurement of liquid film thickness, wall shear stress and gas flow turbulence of horizontal wavy two-phase flow. Int. J. Multiphase Flow 15 (3), 421–431.
Han, H., Gabriel, K., 2007. A numerical study of entrainment mechanism in axisymmetric annular gas–liquid flow. J. Fluids Eng. 129 (3), 293.
Harms, T.M., Li, D., Groll, E.a., Braun, J.E., 2003. A void fraction model for annular flow in horizontal tubes. Int. J. Heat Mass Transfer 46 (21), 4051–4057.
Herrmann, M., 2010. A parallel Eulerian interface tracking/Lagrangian point particle multi-scale coupling procedure. J. Comput. Phys. 229 (3), 745–759.
Hewitt, G.F., Jayanti, S., Hope, C.B., 1990. Structure of thin liquid films in gas–liquid horizontal flow. Int. J. Multiphase Flow 16 (6), 951–957.
Hoogendoorn, C., 1959. Gas–liquid flow in horizontal pipes. Chem. Eng. Sci. 9 (4), 205–217.
Hu, B., Nuland, S., Lawrence, C., 2013. Phase distribution and interface structure of gas–liquid stratified wavy flows in a large-diameter high-pressure pipeline. In: 8th International Conference on Multiphase Flow, Jeju, Korea.
Hurlburt, E., Newell, T., 1996. Optical measurement of liquid film thickness and wave velocity in liquid film flows. Exp. Fluids 21 (5), 357–362.
Hurlburt, E.T., Newell, T.a., 2000. Prediction of the circumferential film thickness distribution in horizontal annular gas–liquid flow. J. Fluids Eng. 122 (2), 396.
Issa, R.I., Kempf, M.H.W., 2003. Simulation of slug flow in horizontal and nearly horizontal pipes with the two-fluid model. Int. J. Multiphase Flow 29 (1), 69–95.
Jacowitz, L., Brodkey, R.S., 1964. An analysis of geometry and pressure drop for the horizontal, annular, two-phase flow of water and air in the entrance region of a pipe. Chem. Eng. Sci. 19 (4), 261–274.
Jayanti, S., Hewitt, G., White, S., 1990a. Time-dependent behaviour of the liquid film in horizontal annular flow. Int. J. Multiphase Flow 16 (6), 1097–1116.
Jayanti, S., Wilkes, N.S., Clarke, D.S., Hewitt, G.F., 1990b. The prediction of turbulent flows over roughened surfaces and its application to interpretation of mechanisms of horizontal annular flow. Proc. Roy. Soc. A: Math. Phys. Eng. Sci. 431 (1881), 71–88.
Kadambi, V., 1982. Stability of annular flow in horizontal tubes. Int. J. Multiphase Flow 8 (4), 311–328.
Kang, S., Choi, H., 2000. Active wall motions for skin-friction drag reduction. Phys. Fluids 12 (12), 3301.
Kosterin, S., 1949. An investigation of the influence of the diameter and inclination of a tube on the hydraulic resistance and flow structure of gas–liquid mixtures. Izvest. Akad. Nauk. SSSR, Otdel Tekh Nauk 12, 1824–1830.
Krasiakova, L., 1957. Some characteristics of the flow of a two phase mixture in a horizontal pipe. Atom. Energy Res. Establish.
Lakehal, D., Fulgosi, M., Yadigaroglu, G., Banerjee, S., 2003. Direct numerical simulation of turbulent heat transfer across a mobile, sheared gas–liquid interface. J. Heat Transfer 125 (6), 1129–1139.
Laurinat, J., Hanratty, T., 1982.Studies of the Effects of Pipe Size on Horizontal Annular Two-Phase Flows, Ph.D. Thesis, University of Illinois, Urbana.
Laurinat, J., Hanratty, T., Jepson, W., 1985. Film thickness distribution for gas–liquid annular flow in a horizontal pipe. PhysicoChem. Hydrodynam. 6, 179–195.
Lin, T., Jones, O., Lahey, R., Block, R., Murase, M., 1985. Film thickness measurements and modelling in horizontal annular flows. PhysicoChem. Hydrodynam. 6, 197–206.
Lombardi, P., De Angelis, V., Banerjee, S., 1996. Direct numerical simulation of near-interface turbulence in coupled gas–liquid flow. Phys. Fluids 8 (6), 1643.
Lu, J., Fernandez, A., Tryggvason, G., 2005. The effect of bubbles on the wall drag in a turbulent channel flow. Phys. Fluids 17 (9), 095102.
Mandhane, J., Gregory, G., Aziz, K., 1974. A flow pattern map for gas–liquid flow in horizontal pipes. Int. J. Multiphase Flow 1 (4), 537–553.
Martinelli, R., Nelson, D., 1948. Prediction of pressure drop during forced-circulation boiling of water. Trans. Asme 70 (6), 695–702.
McCaslin, J.O., Desjardins, O., 2014. A localized re-initialization equation for the conservative level set method. J. Comput. Phys. 262, 408–426.
Meyer, M., Devesa, A., Hickel, S., Hu, X., Adams, N., 2010. A conservative immersed interface method for Large-Eddy Simulation of incompressible flows. J. Comput. Phys. 229 (18), 6300–6317.
Moreno Quibén, J., Thome, J.R., 2007. Flow pattern based two-phase frictional pressure drop model for horizontal tubes – Part II: New phenomenological model. Int. J. Heat Fluid Flow 28 (5), 1060–1072.
Murai, Y., Fukuda, H., Oishi, Y., Kodama, Y., Yamamoto, F., 2007. Skin friction reduction by large air bubbles in a horizontal channel flow. Int. J. Multiphase Flow 33 (2), 147–163.
Nagrath, S., Jansen, K.E., Lahey, R.T., 2005. Computation of incompressible bubble dynamics with a stabilized finite element level set method. Comput. Methods Appl. Mech. Eng. 194 (42–44), 4565–4587.
Ooms, G., Poesio, P., 2003. Stationary core-annular flow through a horizontal pipe. Phys. Rev. E 68 (6), 066301.
Ooms, G., Segal, A., Vanderwees, A., Meerhoff, R., Oliemans, R., 1983. A theoretical model for core-annular flow of a very viscous oil core and a water annulus through a horizontal pipe. Int. J. Multiphase Flow 10 (1), 41–60.
Ooms, G., Vuik, C., Poesio, P., 2007. Core-annular flow through a horizontal pipe: hydrodynamic counterbalancing of buoyancy force on core. Phys. Fluids 19 (9), 092103.
Ooms, G., Pourquie, M., Poesio, P., 2012. Numerical study of eccentric core-annular flow. Int. J. Multiphase Flow 42, 74–79.
Owkes, M., Desjardins, O., 2013. A discontinuous Galerkin conservative level set scheme for interface capturing in multiphase flows. J. Comput. Phys. 249 (1), 275–302.
Öztürk, O.C., Marchand, M., Berlandis, J.-p., Lance, M., 2013. Experimental and analytical investigation of various horizontal two-phase flow regimes. In: 8th International Conference on Multiphase Flow, Jeju, Korea, pp. 1–7.
Paras, S., Karabelas, A., 1991a. Properties of the liquid layer in horizontal annular flow. Int. J. Multiphase Flow 17 (4), 439–454.
Paras, S.V., Karabelas, A.J., 1991b. Droplet entrainment and deposition in horizontal annular flow. Int. J. Multiphase Flow 17 (4), 455–468.
Pepiot, P., Desjardins, O., 2012. Numerical analysis of the dynamics of two- and three-dimensional fluidized bed reactors using an Euler–Lagrange approach. Powder Technol. 220, 104–121.
Pope, S.B., 2000. Turbulent Flows. Cambridge University Press.
Reboux, S., Sagaut, P., Lakehal, D., 2006. Large-eddy simulation of sheared interfacial flow. Phys. Fluids 18 (10), 105105.
Rodriguez, D., Shedd, T.A., 2004. Entrainment of gas in the liquid film of horizontal, annular, two-phase flow. Int. J. Multiphase Flow 30 (6), 565–583.
Russell, T.W.F., Lamb, D.E., 1965. Flow mechanism of two-phase annular flow. Canad. J. Chem. Eng. 43 (5), 237–245.
Schubring, D., Shedd, T., 2008. Wave behavior in horizontal annular air–water flow. Int. J. Multiphase Flow 34 (7), 636–646.
Schubring, D., Shedd, T., 2009a. Prediction of wall shear for horizontal annular air–water flow. Int. J. Heat Mass Transfer 52 (1–2), 200–209.
Schubring, D., Shedd, T., 2009b. Critical friction factor modeling of horizontal annular base film thickness. Int. J. Multiphase Flow 35 (4), 389–397.
Schubring, D., Shedd, T., 2011. A model for pressure loss, film thickness, and entrained fraction for gas–liquid annular flow. Int. J. Heat Fluid Flow 32 (3), 730–739.
Schubring, D., Ashwood, A., Shedd, T., Hurlburt, E., 2010a. Planar laser-induced fluorescence (PLIF) measurements of liquid film thickness in annular flow. Part I: Methods and data. Int. J. Multiphase Flow 36 (10), 815–824.
Schubring, D., Shedd, T., Hurlburt, E., 2010b. Planar laser-induced fluorescence (PLIF) measurements of liquid film thickness in annular flow. Part II: Analysis and comparison to models. Int. J. Multiphase Flow 36 (10), 825–835.
Serdar Kaya, A., Tom Chen, X., Sarica, C., Brill, J.P., 2000. Investigation of transition from annular to intermittent flow in pipes. J. Energy Resour. Technol. 122 (1), 22.
Shedd, T.a., Newell, T.a., 2004. Characteristics of the liquid film and pressure drop in horizontal, annular, two-phase flow through round, square and triangular tubes. J. Fluids Eng. 126 (5), 807.
Simmons, M.J.H., Hanratty, T.J., 2001. Droplet size measurements in horizontal annular gas–liquid flow. Int. J. Multiphase Flow 27 (5), 861–883.
Solbakken, S., Andersson, H.I., 2005. Direct numerical simulation of lubricated channel flow. Fluid Dynam. Res. 37 (3), 203–230.
Sutharshan, B., Kawaji, M., Ousaka, A., 1995. Measurement of circumferential and axial liquid film velocities in horizontal annular flow. Int. J. Multiphase Flow 21 (2), 193–206.
Taitel, Y., Dukler, A.E., 1976. A model for predicting flow regime transitions in horizontal and near horizontal gas–liquid flow. AIChE J. 22 (1), 47–55.
Tandon, T.N., Varma, H.K., Gupta, C.P., 1985. A void fraction model for annular two-phase flow. Int. J. Heat Mass Transfer 28 (I), 191–198.
van't Westende, J., Belt, R., Portela, L., Mudde, R., Oliemans, R., 2007. Effect of secondary flow on droplet distribution and deposition in horizontal annular pipe flow. Int. J. Multiphase Flow 33 (1), 67–85.
Williams, L., 1990. Effect of Pipe Diameter on Horizontal Annular Two-Phase Flow. Ph.D. Thesis, University of Illinois, Urbana.
Woldesemayat, M.a., Ghajar, A.J., 2007. Comparison of void fraction correlations for different flow patterns in horizontal and upward inclined pipes. Int. J. Multiphase Flow 33 (4), 347–370.